Measurement 258 (2026) 119331

Contents lists available at ScienceDirect

Measurement

journal homepage: www.elsevier.com/locate/measurement

# Improved residual stress evaluation with Hole-Drilling and DIC through the L-curve tool and super-resolution along depth

Tommaso Grossi [a],[*], Paolo Neri [b], Ciro Santus [b]

[a] TeCIP Institute, Scuola Superiore Sant'Anna, Pisa, Italy
[b] Dipartimento di Ingegneria Civile e Industriale, Università di Pisa, Pisa, Italy

## ARTICLE INFO

*Keywords:*
Residual stress
Hole-drilling
Digital image correlation
Full-field
Regularization

## ABSTRACT

Full-field methods such as Electronic Speckle Pattern Interferometry (ESPI) and Digital Image Correlation (DIC) emerge as promising alternatives to strain rosette in the hole-drilling method, each with its own advantages and limitations. In particular, DIC stands out as a method requiring minimal (and cheap) specimen preparation; however, its sensitivity is approximately one order of magnitude lower than that of conventional strain gauge techniques.

We address two fundamental questions. First, how can the inverse problem of the hole-drilling method be systematically approached outside the well-established framework of ASTM E837, which provides users with comprehensive guidance, including automated regularization procedures? Second, thanks to full-field measurement techniques, is it possible to retrieve stress distributions at a spatial resolution finer than the drilling step?

We revisit the theoretical development of the inverse problem, aiming to directly identify the residual stresses from raw images, without intermediate pre-processing of the displacement fields. We introduce the L-curve method – well established in other scientific domains – as a rational tool for the choice of the regularization parameter. Finally, we show that, in principle, it would be possible to identify the entire stress distribution from a single drilling increment. We perform a deep rolling treatment on an aluminum specimen and compare the residual stresses identified using both a strain gauge rosette and DIC.

We demonstrate that the proposed framework yields results comparable to those obtained using strain gauge rosettes, while minimizing user-dependent arbitrariness. Furthermore, we show that depth super-resolution of at least a factor of two is already achievable with current technological capabilities.

## 1. Introduction

### 1.1. Hole-drilling method and full-field measurements

The hole-drilling method (HDM) remains a cornerstone in the experimental identification of near-surface residual stress fields, particularly due to its partially non-destructive nature and its adaptability across a wide spectrum of engineering materials and applications. Originally conceptualized by Mathar [1] in the early 20th century, the method is now systematically codified in the ASTM E837 standard [2]. Central to modern implementations is the integral method introduced by Schajer [3–5], which marked a pivotal shift in the analysis of non-uniform residual stress distributions as a function of depth, through the incorporation of numerical calibration functions into the inverse problem. A comprehensive overview and an in-depth survey of the relevant literature can be found in Chapter 2 of Schajer's book [6].

The standardized testing method currently in use is based on the strain gauge (SG) configuration originally proposed by Rendler and Vigness in 1966 [7], which has then become the default strain measurement method in the ASTM standard. Traditional strain-gauge-based measurements offer high sensitivity and are mature in terms of instrumentation and interpretation. However, it is important to note that they involve a significant setup time and cost, and are somewhat dependent on operator skill, which can make them impractical when a large number of tests are required. Optical methods such as Electronic Speckle Pattern Interferometry (ESPI) [8–10] and Digital Image Correlation (DIC) have gained traction due to their ability to acquire full-field displacement maps over the specimen surface. While ESPI offers exceptional sensitivity [11] via coherent light interference, its use outside research laboratories is limited by its requirements in terms of vibration isolation. On the other hand, DIC, either in a 2D [12–15] or a 3D [16–18] setup, by leveraging optical texture and image tracking

---

[*] Corresponding author.
*E-mail address:* tommaso.grossi@santannapisa.it (T. Grossi).

https://doi.org/10.1016/j.measurement.2025.119331
Received 9 July 2025; Received in revised form 16 September 2025; Accepted 13 October 2025

algorithms, provides a generally more robust approach for industrial measurements, although at the cost of a reduced sensitivity [19].

Initial DIC implementations were often restricted to uniform stress analyses due to resolution constraints [12,13]. These studies provided critical validation against classical strain-gauge measurements. However, subsequent advancements in hardware and software have enabled application of the integral method within the DIC framework [14,20, 21]

### 1.2. Contributions and related work

The ASTM E837 standard currently incorporates all the advancements introduced over the years through the work of Schajer. In particular, it provides calibration functions for constructing the sensitivity matrices corresponding to specimens of varying thicknesses and different types of strain gauge rosettes, for any drilling step sequence [22]. Additionally, the user is equipped with a method for rationally applying Tikhonov regularization, aimed at mitigating the high sensitivity of the inverse problem to measurement errors in the recorded strains [23].

When alternative full-field measurement methods are employed, a straightforward approach consists in using *virtual strain gauges* to extract the three strain values that would have been obtained with a physical strain gauge rosette, thereby enabling the application of the classical inversion algorithm [24]. However, it is evident that this approach is not advantageous when using DIC: the accuracy of the measured strain values is at least an order of magnitude lower than that of conventional strain gauges, and this reduced precision will be proportionally reflected – given the linear nature of the problem – in the identification of residual stresses, which is already a challenging task even with strain gauges.

When choosing to utilize the full displacement field for the inversion of the problem, two main approaches emerge. The first one stems by the work of Schajer and Steinzig on ESPI [9] and was later adapted to DIC by Schajer et al. [21,25]. It involves a two-step process: displacement fields are first independently identified using standard DIC algorithms (usually exploiting the correlation of many small local *subsets* extracted from the recorded images, although also global methods can be exploited), and subsequently integrated over appropriate domains so as to conform to the same formalism used for strain gauges. Very interestingly, this approach also enables the automatic compensation of certain measurement artifacts associated with the employed full-field techniques. This approach, with suitably adapted calibration functions, enables continued adherence to the ASTM standard, and it stands out for its ease of use, particularly in cases where the residual stress analyst prefers to employ external, native software tools to identify displacement fields from the captured images. On the other hand, this approach requires the consecutive and sequential resolution of two inverse problems. As demonstrated in [26,27], it is often advantageous in inverse problems to perform a single, unified inversion controlled by a single regularization parameter, whose bias is both well-defined and accessible to the user. Otherwise, biases introduced during the first inversion step – such as in the estimation of displacements that maximize image correlation – may propagate into the subsequent stress identification process in a manner that is not analytically quantifiable and that may negatively affects results, as shown in [18].

The second approach was proposed by Baldi in 2019 [14] and differs from the aforementioned method precisely in this respect: it solves a *single inverse problem* that directly identifies the residual stresses in the material from the captured images. More specifically, by leveraging the known calibration functions that relate the relaxed residual stresses – induced by the introduction of the hole – to the resulting displacement fields, this method formulates an optimization problem. The objective is to find the residual stress distribution that maximizes the correlation between the undeformed reference image and the deformed images acquired at incremental drilling steps.

In doing so, the correlation is performed simultaneously for all pixels within the domain of interest and across all stored images, which formally classifies this algorithm among the *global* DIC methods. In this work, we draw inspiration from this second approach, demonstrating that it can yield results comparable to those obtained using strain gauge rosettes, while maintaining a rigorous approach to problem regularization—and, in fact, enabling the potential introduction of spatial super-resolution along the depth direction.

Tikhonov regularization must be complemented by a rational criterion for selecting the appropriate level of regularization. For example, the ASTM standard recommends the use of Morozov's discrepancy principle [28], which requires knowledge of the random measurement error. To this end, the standard also provides an algorithm for estimating this error directly from strain gauge data. Such an algorithm is currently lacking for the direct inversion of the hole-drilling problem using DIC.

An interesting feature of the integral method using strain gauge rosettes is that the sparsity of the data inherently constrains the maximum number of degrees of freedom in the stress basis used to represent the solution to the number of drilling steps. Specifically, the method yields three strain values per step, resulting in a total of $3n$ measured values for $n$ drilling increments. This, in turn, limits the number of stress coefficients that can be identified to at most $3n$ – that is, $n$ coefficients for each stress component – unless additional physical constraints are introduced. In practice, using more stress coefficients than strain measurements results in an under-determined system—intuitively, a short and wide rectangular matrix. Although this may appear to be an intrinsic limitation of the integral method, *it is not*. In contrast, the vast amount of data obtained through full-field methods renders the system highly over-determined, *even when the number of stress coefficients exceeds the number of drilling steps*.

The main contributions of this paper are outlined as follows:

1. We present a *global* DIC algorithm using an *Eulerian* approach (in contrast with the Lagrangian one used in [14]) based on a *single* annular subset of pixels, formulating an optimization problem to determine the stress values that *simultaneously minimize* the discrepancy between multiple simulated and experimental images.
2. We show that the application of the Morozov discrepancy principle to the inversion of the hole-drilling problem using DIC – as suggested in [14] – is not straightforward, being both unclear and challenging. This is primarily due to the large residuals caused by drilling by-products that fall within the field of view, which far exceed the measurement noise associated with the intensity of individual pixels. In other words, the structure of the error is fundamentally different from that of electrical noise in strain gauge measurements. Instead, we adopt from the inverse problem literature the concept of the L-curve [29], which enables a rational selection of the regularization parameter without requiring prior knowledge of the error level present in the data.
3. We show that, in theory, it is possible to measure the entire distribution of non-uniform residual stresses – with a fairly arbitrary number of degrees of freedom – from a single drilling increment, provided that the corresponding measurements are sufficiently accurate. We also demonstrate that, although the required level of accuracy currently exceeds the capabilities of the state of the art, it is already feasible to achieve a super-resolution of at least a factor of two, yielding appreciable results and a significant reduction in testing time.
4. We complement the theoretical discussion with experimental validation, performed by applying a deep rolling treatment to an aluminum specimen and comparing the DIC results with those obtained from tests using strain gauge–based strain measurements. We designed a measurement system mounted on a numerically controlled machine, capable of alternating in an automated and highly repeatable manner between image acquisition with the camera and drilling of the subsequent increment.

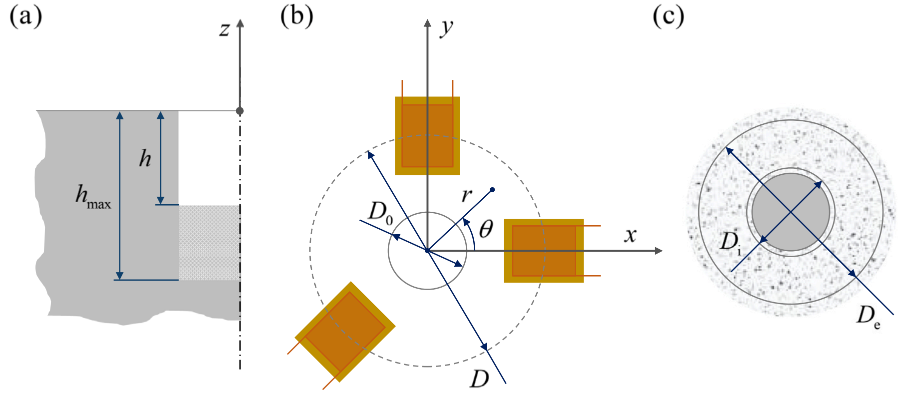

**Fig. 1.** Hole-drilling method: variables and geometrical quantities. (a) Here, $h$ denotes the *physical depth* of the drilled hole, corresponding to the total depth achieved at a given drilling increment, while $z$ indicates a *spatial coordinate* aligned with the specimen thickness and oriented according to the right-hand rule. (b) Reference system and variable definitions for the strain-gauge formalism. (c) Variable definitions for the DIC formalism.

## 2. Theory

### 2.1. Hole-drilling method

When a hole is drilled into a body made of a linear elastic material and the induced deformations remain purely elastic, the system behaves linearly, allowing the application of Bueckner's principle of superposition [30]. Under the assumption of plane stress, Schajer [3] introduced a computationally simpler analogue to the actual problem. The resulting displacement field from drilling can be modeled by applying boundary tractions, equal in magnitude but opposite in direction to the relaxed residual stresses, to the holed geometry. This alternate framework allows simulation of the produced displacement fields using standard finite element tools. The critical assumption is that, at each depth, the residual stress is homogeneous across the plane parallel to the surface (the $xy$ plane in Fig. 1) over an area approximately matching the diameter $D_0$ of the drilled hole.

If the residual stress field changes significantly with depth $z$, it can be described using a set of $n$ independent basis functions of the depth variable $z$, linearly combined to approximate one of the actual residual stress components $\sigma(z)$. This approach presumes that the chosen basis spans the set of stress profiles relevant to the material in question. For example, the Power Series Method [4] is one such implementation, using polynomial terms where the unknowns correspond to the polynomial coefficients.

Alternatively, the well-established Integral Method splits the depth interval $[0, h_{\max}]$ into smaller segments $[h_{i-1}, h_i]$ and associate each of them with an indicator function $\chi_{[h_{i-1},h_i]}(z)$ that equals 1 inside the segment and 0 elsewhere. Hence, each residual stress component is assumed to be constant within each interval, and the unknowns are the stress levels $s_i$ in each zone:

$$\sigma_{xx}(z) = \sum_{i=1}^{n} s_{xx,i}\, \chi_{[h_{i-1},h_i]}(z) \tag{1}$$

The same holds for the other components $\sigma_{yy}$ and $\sigma_{xy}$, having stress coefficients $s_{yy}$ and $s_{xy}$, respectively. In other works [31–33], linear splines have also been proposed to represent residual stresses.

Given the linearity of the problem, it is possible to separately evaluate the effect of the stress tensor acting within a specific depth segment – characterized by a triplet $\{s_{xx,i}, s_{yy,i}, s_{xy,i}\}$ – on the resulting displacement field generated around a hole of depth $h$. Subsequently, the overall effect due to a generic distribution of residual stresses can be obtained through the linear superposition of the individual results.

The linearity of the problem has another important consequence. Due to the axial symmetry of the problem, the general solution can be expanded in a Fourier series, resulting in mutually independent subproblems. Owing to the properties of the stress tensor, the applied tractions in the problem contain only a constant component and a component varying as $2\theta$; consequently, only these two corresponding Fourier components of the solution are nonzero. Therefore, in cylindrical coordinates, the displacement fields produced *by a single basis function* can be expressed in adimensional form as (see [25]):

$$\begin{aligned}
\frac{u_r(r,\theta,h)}{D_0} &= \frac{1}{E}\left[\frac{s_{xx}+s_{yy}}{2}\, a_r(r,h) + \left(\frac{s_{xx}-s_{yy}}{2}\cos(2\theta) + s_{xy}\sin(2\theta)\right) b_r(r,h)\right] \\
\frac{u_\theta(r,\theta,h)}{D_0} &= \frac{1}{E}\left[\left(\frac{s_{xx}-s_{yy}}{2}\sin(2\theta) - 2s_{xy}\cos(2\theta)\right) b_\theta(r,h)\right]
\end{aligned} \tag{2}$$

where $a_r(r,h)$, $b_r(r,h)$ and $b_\theta(r,h)$ are the functional equivalents of calibration coefficients for the strain gauge formalism, which also depend on the material's Poisson ratio and must be evaluated with finite-element (FE) analyses. In other words, these represent the exact solution corresponding to a single Fourier mode, which must then be expanded in the angular coordinate $\theta$. As such, they depend solely on the radial distance from the hole axis and on the hole depth. In the case of a blind hole, these solutions can only be determined through finite element analysis. In practice, for each basis function and each physical hole depth $h$, we perform a FE simulation in which the basis function is applied as a traction on the hole walls, and the corresponding surface displacements are determined. The function $a_r(r,h)$ corresponds to the radial displacements obtained under an equibiaxial (i.e., axisymmetric) loading, whereas the functions $b_r(r,h)$ and $b_\theta(r,h)$ correspond, respectively, to the radial and circumferential displacements obtained under a pure shear loading. The use of the letters $a$ and $b$ is inspired to the conventional notation of the calibration constants $A$ and $B$ for the same two types of loading in the strain-gauge formalism [4]. The use of Fourier elements (such as SOLID272 in ANSYS) allows $a_r(r,h)$, $b_r(r,h)$ and $b_\theta(r,h)$ to be determined through 2D FE models, with high computational efficiency. Further details of the procedure are available in [34].

As noted in [14], Eq. (2) is also a highly memory-efficient strategy for storing the displacement fields as functions of the radial coordinate only, rather than at each pixel (typically numbering in the millions) of the camera sensor.

Eq. (2) can be expressed *for every basis function* employed to represent the residual stresses, each associated with the corresponding functions $a_r(r,h)$, $b_r(r,h)$ and $b_\theta(r,h)$ in a manner analogous to the calibration coefficients in the integral method within the strain gauge formalism, where each stress coefficient is linked to its respective effect on the measured strain at a given depth $h$. This complicates the compactness of the problem's notation in the case of DIC, since each stress coefficient and each hole depth $h$ correspond not to three discrete strain values measured on the strain gauge rosette, but rather to three scalar fields $a_r(r,h)$, $b_r(r,h)$ and $b_\theta(r,h)$ that depend on the distance $r$ from the center of the hole.

In addition to these displacement fields, it is advisable – given their typically low intensity – to also model the presence of typical measurement artifacts associated with DIC, linearly superimposing them onto the physical displacements. In the case of DIC, the magnitude of rigid-body motions resulting from imperfect repositioning of the camera along the optical axis after a drilling increment is often non-negligible for the purpose of residual stress identification. A comprehensive overview of typical DIC-related artifacts can be found in [25]. For example, as done in the present work, the expressions that models the displacement in the $x$ and $y$ directions in the $j$th recorded image, in accordance with Eq. (2), when superimposed with a rigid-body translation $t_{x,j}$ along $x$ and $t_{y,j}$ along $y$ and with a rotation of the camera's reference frame by $\omega_j$, can be written as:

$$\begin{aligned} u_x(r,\theta,h) &= t_{x,j} + u_r(r,\theta,h)\cos(\theta) - \left[u_\theta(r,\theta,h) + r\omega_j\right]\sin(\theta) \\ u_y(r,\theta,h) &= t_{y,j} + u_r(r,\theta,h)\sin(\theta) + \left[u_\theta(r,\theta,h) + r\omega_j\right]\cos(\theta) \end{aligned} \tag{3}$$

As stated above, knowledge of the stress coefficients $\{s_{xx,i}, s_{yy,i}, s_{xy,i}\}$ – together with those related to the measurement artifacts – allows the displacement field to be generated through linear superposition. In practice, this enables the assembly of a linear system of the form

$$\boldsymbol{A}\boldsymbol{s} = \boldsymbol{u} \tag{4}$$

where $\boldsymbol{A}$ is the system matrix containing the displacement responses (influence functions) associated with each stress basis function, $\boldsymbol{s}$ is the vector that stacks the unknown stress coefficients $\{s_{xx,i}, s_{yy,i}, s_{xy,i}\}$ and the artifact coefficients for the $j$th image $\{t_{x,j}, t_{y,j}, \omega_j\}$, and $\boldsymbol{u}$ is a stacking of all measured displacements at various spatial positions and hole depth.

### 2.2. Digital image correlation

DIC is a non-contact optical method widely employed for measuring full-field displacement and strain on the surface of materials. Since its emergence in the 1980s [35–37], DIC has evolved into a powerful tool for experimental mechanics, enabling the analysis of mechanical behavior under static, dynamic, and thermomechanical loading conditions. The reader is referred to the textbook of Schreier et al. [19] for a comprehensive treatment of the method.

In its continuous formulation [38], DIC seeks a kinematic transformation $\phi(\boldsymbol{x}, \boldsymbol{u}(\boldsymbol{x})) = \boldsymbol{x} + \boldsymbol{u}(\boldsymbol{x})$ of any point $\boldsymbol{x}$ within a region $\Omega$ on the surface of a test specimen, represented by a displacement vector field $\boldsymbol{u}(\boldsymbol{x})$. This is done by comparing grayscale digital images captured before and after deformation—denoted, respectively, as $f(\boldsymbol{x})$ and $g(\boldsymbol{x})$. The main goal of DIC is to determine the transformation $\phi(\boldsymbol{x}, \boldsymbol{u}(\boldsymbol{x}))$ that best satisfies the equation of gray level conservation:

$$r(\boldsymbol{x}, \boldsymbol{u}(\boldsymbol{x})) = f(\boldsymbol{x}) - g\circ\phi(\boldsymbol{x}, \boldsymbol{u}(\boldsymbol{x})) = 0, \quad \forall \boldsymbol{x} \in \Omega \tag{5}$$

where $f(\boldsymbol{x})$ denotes the grayscale intensity at point $\boldsymbol{x}$ in the reference image, while $g\circ\phi(\boldsymbol{x}, \boldsymbol{u})$ represents the intensity in the deformed image at a location that has been changed by the kinematic transformation $\phi(\boldsymbol{x}, \boldsymbol{u}(\boldsymbol{x}))$. See Fig. 2 for an example of reference and deformed images.

Eq. (5) is a classical inverse problem, in which the forward operator –describing how an image is deformed by a given displacement field – is analytically known, and the objective is to reconstruct the displacement field itself from a pair of images. As in the case of residual stress identification, it becomes necessary to approximate the displacement field in a finite-dimensional space, i.e., by expressing it as a linear combination of various basis functions.

From this formulation, several approaches emerge. In the case of subset-based methods, displacements are represented as a linear combination of low-order polynomials defined over small image patches (*subsets*), and the inverse problem is solved independently within each subset. Crucially, no continuity is enforced across the boundaries of adjacent subsets, which simplifies computation but may introduce discontinuities in the reconstructed field. In the case of global methods, the displacement fields are expressed – analogously to finite element formulations – as a function of a finite set of nodal displacements, which in turn generate the entire field through the shape functions associated with the chosen elements. This formulation inherently enforces continuity across the entire domain. As a result, similar to a mechanical finite element model, the inverse problem must be solved globally in a single step, rather than on independent subsets. These two broad classes encompass the majority of algorithms implemented in DIC software for displacement fields identification. From the resulting displacement fields, Eq. (4) can then be solved, as done in the approaches performing a two-step inversion.

Actually, as shown in [12], Eq. (4) *already* provides a projection of the admissible displacement field onto a finite-dimensional basis indexed solely by the coefficients of the vector $\boldsymbol{s}$. In other words, the displacement field is already available as a function of a *finite* number of stress and artifact coefficients, making it possible to directly solve Eq. (5) by assuming this specific parametric form for $\phi(\boldsymbol{x}, \boldsymbol{u}(\boldsymbol{x}))$. In other words, Eq. (5) becomes:

$$r(\boldsymbol{x}, \boldsymbol{s}) = f(\boldsymbol{x}) - g\circ\phi(\boldsymbol{x}, \boldsymbol{s}) = 0, \quad \forall \boldsymbol{x} \in \Omega \tag{6}$$

which redefines the DIC problem as an optimization in terms of the stress and artifact coefficients $\boldsymbol{s}$ only.

In fact, when $n_{\text{steps}}$ drilling steps are performed, one reference image and $n_{\text{steps}}$ deformed images are available; the displacement fields giving rise to the latter all depend on the same set of stress and artifact coefficients $\boldsymbol{s}$. Therefore, the image correlation must be carried out simultaneously over the entire set of deformed images:

$$r_j(\boldsymbol{x}, \boldsymbol{s}) = f(\boldsymbol{x}) - g_j\circ\phi_j(\boldsymbol{x}, \boldsymbol{s}) = 0, \quad \forall \boldsymbol{x} \in \Omega, \forall j \in [1 \dots n_{\text{steps}}] \tag{7}$$

At most, in principle, one could exploit the lower-triangular structure of the system arising from the application of the integral method—as also proposed in [14]. However, this approach does not permit the application of Tikhonov regularization and will therefore not be considered in the present work.

Since the images $f$ and $g_j$ are available only as discrete samples at a finite number of pixels, Eq. (6) can be enforced only at a finite set of spatial positions $\boldsymbol{x}$. Moreover, measurement noise, the presence of inadequately modeled artifacts, and the intrusion of drilling debris into the image field make the exact satisfaction of Eq. (6) impossible.

Consequently, the problem is solved in a least-squares sense over a finite set of spatial positions $\boldsymbol{x}_i$ corresponding to the $n_{\text{pixels}}$ pixels of the camera sensor:

$$\begin{aligned} \boldsymbol{s}^\dagger &= \arg\min_{\boldsymbol{s}} \sum_{j=1}^{n_{\text{steps}}} \sum_{i=1}^{n_{\text{pixels}}} r_j(\boldsymbol{x}_i, \boldsymbol{s})^2 \\ &= \arg\min_{\boldsymbol{s}} \sum_{j=1}^{n_{\text{steps}}} \left\| \boldsymbol{r}_j(\boldsymbol{s}) \right\|^2 \\ &= \arg\min_{\boldsymbol{s}} \|\boldsymbol{r}(\boldsymbol{s})\|^2 \\ &= \arg\min_{\boldsymbol{s}} \Theta(\boldsymbol{s}) \end{aligned} \tag{8}$$

where we have naturally defined:

$$\boldsymbol{r}_j(\boldsymbol{s}) \triangleq \left[ r_j(\boldsymbol{x}_1, \boldsymbol{s}) \dots r_j(\boldsymbol{x}_i, \boldsymbol{s}) \dots r_j(\boldsymbol{x}_{n_{\text{pixels}}}, \boldsymbol{s}) \right] \tag{9}$$

$$\boldsymbol{r}(\boldsymbol{s}) \triangleq \left[ \boldsymbol{r}_1(\boldsymbol{x}_1, \boldsymbol{s}) \dots \boldsymbol{r}_j(\boldsymbol{x}_i, \boldsymbol{s}) \dots \boldsymbol{r}_{n_{\text{steps}}}(\boldsymbol{x}_{n_{\text{pixels}}}, \boldsymbol{s}) \right] \tag{10}$$

$$\Theta(\boldsymbol{s}) \triangleq \|\boldsymbol{r}(\boldsymbol{s})\|^2 \tag{11}$$

In other words, $\boldsymbol{r}_j(\boldsymbol{s})$ is the vector of residuals computed over all pixels of image $j$, while $\boldsymbol{r}(\boldsymbol{s})$ is a $n_{\text{steps}} \times n_{\text{pixels}}$ matrix obtained by stacking all the $\boldsymbol{r}_j(\boldsymbol{s})$ vectors along a new dimension of size $n_{\text{steps}}$.

Eq. (7) would be commonly referred to as a *Lagrangian formulation* of the DIC problem, since – by analogy with terminology from fluid

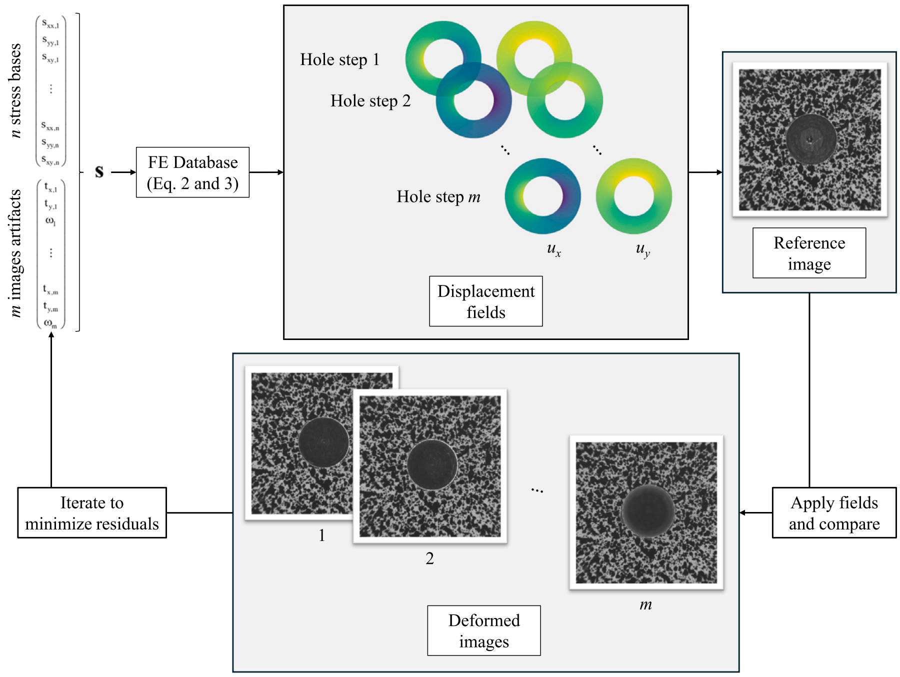

**Fig. 2.** Depiction of the global correlation problem for the hole-drilling method with DIC. One seeks the residual stress values that maximize the correlation between the reference and the deformed images, by knowing the displacement fields produced by the introduction of the hole in a stressed specimen. Given the natural expression of the domain in cylindrical coordinates (as in Eq. (2)), the DIC problem is solved over an annular region surrounding the hole.

dynamics – the domain is fixed on the reference image $f$, and the new positions of the pixels from $f$ are sought in the deformed image $g$. Alternatively, Eq. (7) can be rewritten in the so-called *Eulerian formulation*, in which the relationship between the reference and deformed images is inverted:

$$r_j(\boldsymbol{x}, \boldsymbol{s}) = f \circ \phi_j^{-1}(\boldsymbol{x}, \boldsymbol{s}) - g_j(\boldsymbol{x}) = 0, \quad \forall \boldsymbol{x} \in \Omega, \forall j \in [1 \dots n_{\text{steps}}] \tag{12}$$

where the inverse of the kinematic transformation $\phi(\boldsymbol{x}, \boldsymbol{u}(\boldsymbol{x}))$ can simply be written as:

$$\phi^{-1}(\boldsymbol{x}, \boldsymbol{u}(\boldsymbol{x})) = \boldsymbol{x} - \boldsymbol{u}(\boldsymbol{x}) \tag{13}$$

In the case of Eq. (13), we can define $\phi(\boldsymbol{x}, \boldsymbol{s})$ as a stack of the individual transformations $\phi_j(\boldsymbol{x}, \boldsymbol{s})$ along a new dimension. Then, defining the residuals $r_j(\boldsymbol{x}, \boldsymbol{s})$ as in Eqs. (12), (8) still holds.

Even though the two formulations are essentially equivalent in principle, the present work adopts the Eulerian approach, for computational convenience. In fact, to achieve subpixel accuracy – which is highly desirable given the small displacements involved in the hole-drilling method – all expressions involving $g_j \circ \phi_j(\boldsymbol{x}, \boldsymbol{s})$ require interpolation of the image $g_j$ at non-integer pixel locations; for $n_{\text{steps}}$ drilling steps, $n_{\text{steps}}$ interpolating functions must be built. In contrast, within the Eulerian approach, only an interpolation of the reference image $f$ alone is needed, in which the original positions of the pixels belonging to the deformed images will subsequently be sought, all at the same time.

Eq. (8) defines a nonlinear optimization problem, which is solved iteratively until a local minimum is found. To this end, it is useful to report the analytical expression of the gradient of the objective functional $\Theta(s)$ to be optimized:

$$\begin{aligned}\left(\frac{d\Theta}{d\boldsymbol{s}}\right)^T &= 2\,\boldsymbol{r}(\boldsymbol{s})^T \frac{d\boldsymbol{r}}{d\boldsymbol{s}} \\ &= 2\,\boldsymbol{r}(\boldsymbol{s})^T \frac{d\boldsymbol{r}}{d\boldsymbol{u}}\frac{d\boldsymbol{u}}{d\boldsymbol{s}} \\ &= 2\,\boldsymbol{r}(\boldsymbol{s})^T \left.\frac{df}{d\boldsymbol{x}}\right|_{\boldsymbol{x}=\phi^{-1}(\boldsymbol{x},\boldsymbol{s})} \frac{d\phi^{-1}}{d\boldsymbol{u}}\frac{d\boldsymbol{u}}{d\boldsymbol{s}} \\ &= -2\,\boldsymbol{r}(\boldsymbol{s})^T \left.\frac{df}{d\boldsymbol{x}}\right|_{\boldsymbol{x}=\phi^{-1}(\boldsymbol{x},\boldsymbol{s})} \boldsymbol{A}\end{aligned} \tag{14}$$

since $\frac{d\phi^{-1}}{d\boldsymbol{u}} = -\boldsymbol{I}$ and $\frac{d\boldsymbol{u}}{d\boldsymbol{s}} = \boldsymbol{A}$ from Eq. (4). Strictly speaking, in order to adhere to standard tensor multiplication conventions, the matrix $\boldsymbol{A}$ must be arranged as a tensor of dimensions $n_{\text{pixels}} \times n_{\text{steps}} \times 2 \times n_{\text{coeffs}}$; that is, for each of the $n_{\text{coeffs}}$ coefficients describing the solution, $\boldsymbol{A}$ contains, for each of the $n_{\text{steps}}$ deformed images and for each of the $n_{\text{pixels}}$ pixels, the corresponding two displacement components in the $x$ and $y$ directions; when multiplied by $\boldsymbol{s}$ as in Eq. (4), it yields a $\boldsymbol{u}$ displacement tensor having dimensions $n_{\text{pixels}} \times n_{\text{steps}} \times 2$. Analogously, $\boldsymbol{r}(\boldsymbol{s})^T$ is a $n_{\text{pixels}} \times n_{\text{steps}}$ matrix, while $\left.\frac{df}{d\boldsymbol{x}}\right|_{\boldsymbol{x}=\phi^{-1}(\boldsymbol{x},\boldsymbol{s})}$ is a $n_{\text{pixels}} \times n_{\text{steps}} \times 2$ tensor. By following Einstein summation convention and contracting indexes having same dimensions, one correctly obtains[1] a gradient $\left(\frac{d\Theta}{d\boldsymbol{s}}\right)^T$ having dimensions $1 \times n_{\text{coeffs}}$.

In other words, since the matrix $\boldsymbol{A}$ – which encodes the linear relationship between the residual stress coefficients and the corresponding relaxed strains – is known by FE analyses, the gradient of the objective function only requires an interpolation of the reference image $f$ as it appears in the residuals $\boldsymbol{r}_j$ and the interpolation of its spatial gradient, both evaluated at arbitrary non-integer pixel locations.

The optimization of Eq. (8) is iteratively performed using the classical Gauss–Newton method [38], which entails carrying out the iterations of Newton's method:

$$\boldsymbol{s}_{n+1} = \boldsymbol{s}_n - \boldsymbol{H}_s^{-1}(\Theta)\frac{d\Theta}{d\boldsymbol{s}} \tag{15}$$

while approximating the Hessian $\boldsymbol{H}_s$ of $\Theta(s)$ with respect to $\boldsymbol{s}$ as follows:

$$\boldsymbol{H}_s(\Theta) = 2\left(\frac{d\boldsymbol{r}}{d\boldsymbol{s}}^T \frac{d\boldsymbol{r}}{d\boldsymbol{s}} + \boldsymbol{H}_s(\boldsymbol{r})\,\boldsymbol{r}(\boldsymbol{s})\right) \approx 2\left(\frac{d\boldsymbol{r}}{d\boldsymbol{s}}^T \frac{d\boldsymbol{r}}{d\boldsymbol{s}}\right) \tag{16}$$

where the approximation becomes increasingly accurate as the computation is performed closer to an exact fit point, that is, as $\|\boldsymbol{r}(\boldsymbol{s})\| \to 0$. The term $\frac{d\boldsymbol{r}}{d\boldsymbol{s}}^T$ in Eq. (16) is a slight abuse of notation, being it actually three-dimensional; it can be easily expanded as in Eq. (14) to eventually obtain a $n_{\text{coeffs}} \times n_{\text{coeffs}}$ Hessian matrix.

---

[1] For memory access efficiency, it is in fact more convenient to compute the gradient $d\Theta/ds$ by transposing Eq. (14).

Eventually, the proposed Eulerian approach requires only an interpolation over a continuous domain of the *reference* image, which is necessary to evaluate $\boldsymbol{r}(\boldsymbol{s})$, and its gradients, which are needed to compute $\frac{d\boldsymbol{r}}{d\boldsymbol{s}}$. These interpolations are defined once and for all at the beginning of the problem and are merely evaluated at different locations for each iteration step. By computing the coefficients of those interpolators once prior to the optimization process, no further image processing is required during the iterative solution, thereby significantly improving computational efficiency. Additionally, we believe there is another advantage behind this choice: the reference image is considerably cleaner than the deformed images, which are affected by drilling debris and paint scratches. These artifacts introduce more noise into the image interpolation process and – most importantly – into the corresponding gradients. By contrast, the tensor $\boldsymbol{A}$ remains constant once the stress basis, the drilling depths, and the pixel grid of the camera sensor have been specified.

### 2.3. Tikhonov regularization and the L-curve criterion

In the formulation defined by ASTM E837 [2], second-order Tikhonov regularization is employed as a means to reduce the sensitivity of the solution to noise in the input data, at the expense of introducing a smoothness bias in the solution. Specifically, instead of solving the classical least-squares problem (like Eq. (8)), it adds to the residual norm a penalty term based on the norm of the second derivative of the solution, thereby favoring smoother solutions for a given residual magnitude. A thorough analysis of Tikhonov regularization in the hole-drilling method can be found in [26,27].

Formally, let $\boldsymbol{C}$ denote the matrix associated with the linear operator that estimates the second derivative $\boldsymbol{C}\boldsymbol{s}$ of the residual stress distribution using finite differences (as explained in [26]), built by excluding artifact coefficients from the computation. Then, by directly applying the definition of Tikhonov regularization, an alternative optimization problem is defined:

$$\boldsymbol{s}^{\dagger}_{\alpha} = \arg\min_{\boldsymbol{s}} \left[\Theta(\boldsymbol{s}) + \alpha \left\|\boldsymbol{C}\boldsymbol{s}\right\|^2\right] \triangleq \arg\min_{\boldsymbol{s}} \Theta_{\alpha}(\boldsymbol{s}) \tag{17}$$

where $\alpha$ is the so-called *regularization parameter* of the inverse problem. For very small values of $\alpha$, the solution closely approximates the classical least-squares solution; conversely, for large values of $\alpha$, the minimization of the penalty functional dominates the objective, often resulting in unacceptably large residuals. The gradient of $\Theta_{\alpha}(\boldsymbol{s})$ with respect to $\boldsymbol{s}$ can be readily computed:

$$\left(\frac{d\Theta_{\alpha}}{d\boldsymbol{s}}\right)^{T} = -2\,\boldsymbol{r}(\boldsymbol{s})^{T}\,\frac{d\boldsymbol{f}}{d\boldsymbol{x}}\Big|_{\boldsymbol{x}=\boldsymbol{\phi}(\boldsymbol{x},\boldsymbol{s})}\boldsymbol{A} + 2\alpha\,\boldsymbol{s}^{T}\boldsymbol{C}^{T}\boldsymbol{C} \tag{18}$$

and also the corresponding approximated Hessian easily follows from Eq. (18).

Tikhonov regularization must therefore be complemented by a principled criterion for selecting the regularization parameter $\alpha$. One such criterion is the so-called Morozov discrepancy principle, originally introduced in [28] and thoroughly analyzed in [26,27] with regard to its application to residual stress measurements. Assuming that the standard deviation of the error affecting each individual measurement point is known, the Morozov discrepancy principle relies on the statistical consideration that it is highly unlikely for the residual to vanish exactly in the presence of measurement noise. Instead, the principle prescribes increasing the regularization parameter $\alpha$ until the squared norm of the residuals matches its expected value—namely, the mean of a chi-squared distribution with degrees of freedom equal to the number of measurement points.

The Morozov discrepancy principle exhibits favorable mathematical properties [39], provided that the random measurement error is *accurately known* and that it represents the *dominant contribution* to the discrepancy between the measured images and the ones modeled from the reference image. We will show that this is not typically the case for the hole-drilling method when using DIC to measure the displacement fields.

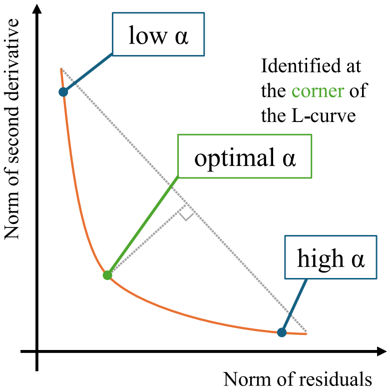

**Fig. 3.** A typical trend of an L-curve in the regularization of an inverse problem is observed. For low values of $\alpha$, the solution yields very small residuals; however, its high sensitivity to measurement errors results in highly oscillatory solutions, characterized by large values of the norm approximating the second derivative of the solution. Conversely, for high values of $\alpha$, the solution primarily favors the minimization of the penalty functional, at the expense of the residuals, which consequently increase. Both of these extremes are likely to deviate significantly from the "true" solution of the problem. The corner of the curve, identified as the point farthest from the line connecting the two endpoints, is used as a heuristic criterion for selecting the value of $\alpha$.

Alternatively, we propose a criterion for the selection of the regularization parameter $\alpha$, known as the *L-curve criterion*. This approach was first introduced by Lawson and Hanson [40], and later popularized by Hansen in the 1990s [29,41,42].

Looking at the structure of Eq. (17), we can identify two key components: the functional $\Theta(\boldsymbol{s})$, which measures the DIC residuals, and a regularization term $\|\boldsymbol{C}\boldsymbol{s}\|^2$ that penalizes the second derivative of the residual stress distribution. When $\alpha$ becomes very large, the optimization prioritizes smoothness, leading to high residuals but a small penalty term. On the other hand, when $\alpha$ is very small, the residuals become small, but the solution may become noisy due to lack of regularization [43].

If we plot $\sqrt{\Theta}$ against $\|\boldsymbol{C}\boldsymbol{s}\|$ for a range of $\alpha$ values, the resulting curve typically takes the shape of an L (see Fig. 3). This L-curve provides a visual and practical way to choose an appropriate $\alpha$: the optimal value is usually found near the corner of the L, where a good balance is struck between minimizing the residuals and keeping the solution smooth. To identify this corner, one simply searches for the point of maximum curvature along the parametric curve. Before doing so, a log–log transformation is applied to the plane to ensure the method is independent of the axes' scaling.

Since computing the curvature requires evaluating the first and second derivatives of the L-curve with respect to $\alpha$, and given that this calculation is highly sensitive to the unavoidable convergence tolerances in the optimization of Eq. (17), its explicit computation is rather delicate and necessitates careful tuning of the numerical parameters involved.

As an alternative, we propose a more expedient method for identifying the corner of the L-curve. We connect the first and last points of the L-curve with a straight line and identify the corner as the point on the curve that *maximizes the distance from this line* (see Fig. 3), which can be easily computed analytically. Very interestingly, we prove in Appendix that this method yields results invariant to the scaling of the Cartesian axes on which the L-curve is defined, a property particularly useful to ignore the units in which the residual norm and the Tikhonov regularization penalty term are expressed.

### 2.4. Algorithm details

In this section, we summarize the operational details of the entire solution algorithm.

1. We capture a single reference image, shot as soon as the drill bit scratches the specimen surface, and we use it to get an estimate of the hole center location through a Hough transform [44], implemented in the `OpenCV` library [45]. As proven in [33], the least squares problem of the hole-drilling method exhibits zero first-order (in Taylor's sense) sensitivity with respect to hole eccentricity when displacement fields are measured on domains symmetric about the $x$ and $y$ axes, as in DIC; hence, the accuracy of this identification is not critical.
2. We select the number of calculation steps for the integral method, which, unless otherwise specified, corresponds to the number of drilling steps. We select the pixels from the deformed images that lie between a minimum and maximum radial coordinate, expressed as multiples of the hole radius; this defines an annular region in which the DIC analysis is conducted, as illustrated in Fig. 2. In the present work, after some preliminary trials, we select pixels between 1.1 and 2.1 times the hole radius. For each basis function and for each hole depth, we solve the corresponding finite element problem and store the resulting functions $a_r(r)$, $b_r(r)$, and $b_\theta(r)$. In our case, leveraging a finite element analysis database described in [34], the three solutions are rapidly reconstructed by linearly superimposing the solutions corresponding to residual stresses modeled as Dirac delta functions acting at given depths. This step is therefore performed without the need to solve a FE model anew, and leads to a complete knowledge of $\boldsymbol{u}(\boldsymbol{s})$, including also the rigid-body motions as in Eq. (3).
3. We build a bicubic interpolation of the reference image $f$ through a cubic convolution algorithm [46], storing coefficients in order to rapidly evaluate both pixel values at non-integer locations and the corresponding gradients.
4. We iteratively solve the optimization problem defined by Eq. (17) with a Gauss–Newton algorithm, starting from a null initial stress distribution and explicitly providing the gradients of the target functional through Eq. (18). Since the latter involves multiplying matrices with dimensions on the order of millions of elements (corresponding to the pixels), we store the relevant data on an NVIDIA RTX 4090 GPU and parallelize the computation, achieving substantial computational gains; for the analyses presented in this work, the use of this GPU allows the entire procedure – from images to residual stresses – to be completed in less than one minute, compared with approximately ten minutes on a CPU. We stop when a given relative convergence tolerance has been exceeded; for the analyses in the present work, a value of $10^{-4}$ has been selected.
5. When the use of the L-curve criterion is required, we solve Eq. (17) over a range of $\alpha$ values between $10^{-6}$ and $10^{6}$, using as the initial guess for each inverse problem the solution obtained for the previous $\alpha$, to the benefit of the number of iterations needed to achieve convergence. Eventually, we identify the corner of the L-curve and find the corresponding $\alpha$, which is used to retrieve the related stress solution.

### 2.5. More DOFs than drilling steps

Let us consider Eq. (2), computed for two different integration intervals of the integral method but at the same depth $h$, for example, the maximum depth in a given experiment. The shape of the resulting displacements remains exactly the same – due to the properties of the Fourier series expansion – but the three functions $a_r(r,h)$, $b_r(r,h)$ and $b_\theta(r,h)$ change. This mathematical detail has a clear physical analogy, also noted by Schajer in [21]: residual stresses near the surface tend to produce displacements localized at the edge of the hole, whereas stresses originally located deeper manifest their effects at larger radial coordinates.

Although it is evident that the three functions exhibit at least a comparable trend along the depth, it is equally clear that their lack of exact collinearity, in principle, allows for a decomposition of the displacement field measured in a *single* image along these components, each corresponding to a stress coefficient. In other words, full-field methods allow overcoming one of the longest-standing limitations of the hole-drilling method—i.e., that the number of calculation points cannot exceed the number of drilling steps. Provided that the measurement accuracy is sufficient to resolve components that are nearly collinear, it would, in principle, be possible to identify a residual stress distribution with an arbitrary number of degrees of freedom from a single hole.

As repeatedly noted in [26,27], such an approach is certainly disadvantageous for measurement quality, since data redundancy always improves the solution accuracy in inverse problems like this. Regardless, it is clear that practical measurements – especially in industrial settings – inevitably involve a trade-off between result quality and the time required to obtain it. In many contexts, there may be a strong incentive to reduce the duration of a single hole-drilling test. Therefore, it is particularly motivating to set this benchmark as a sensitivity target for the method, at which point the hole-drilling technique will have likely reached an insurmountable limit in execution speed: using a single reference image and a single deformed image to identify the entire residual stress distribution.

Through our experimental validation, we will subsequently take stock of the current situation, aiming to understand how far we are from achieving this objective.

## 3. Experimental methods

### 3.1. Deep-rolled specimens

In this research, a residual stress distribution was introduced in a plate of aluminum 7075-T6. This alloy was intentionally chosen to reduce drilling effort and to allow for minor irregularities in the hole shape. As well known, aluminum alloys have a lower Young's modulus compared to steel or other commonly used metal alloys. Additionally, this alloy exhibits a high yield stress, allowing for the development of significant residual stresses, and its tensile response is notably linear within the elastic region. These factors mean that displacements – captured by the DIC camera – are expected to be relatively large, making it well-suited for introducing residual stresses and ensuring accurate measurement.

The deep rolling treatment was applied to a long bar-shaped plate. The features of this specimen have been previously described in [47–51]. The plate's length and shape were specifically designed for a custom test bench that enables the application and removal of a bending load at each drilling step (see Fig. 4).

This test bench was designed for use with hole-drilling and a strain gauge rosette, enabling decoupling of the relaxed strains due to residual stresses from those caused by bending stresses. The availability of this setup was strategic for systematic validation of the hole-drilling method using a strain gauge rosette, which serves here as a reference for evaluating HDM-DIC stress distributions. As shown in Fig. 5, the central region of the plate was deep rolled. The treatment was similar to that described in [52], where the goal was to introduce compressive residual stresses for improving fatigue strength, particularly against fretting fatigue [53]. In the present study, the aim was to create a meaningful stress distribution with a steep gradient near the subsurface, which is not equi-biaxial. The deep rolling tool is a conical, rounded carbide roller pressed against the surface—applicable via a turning machine or machining center. The tool is equipped with a small load cell and a

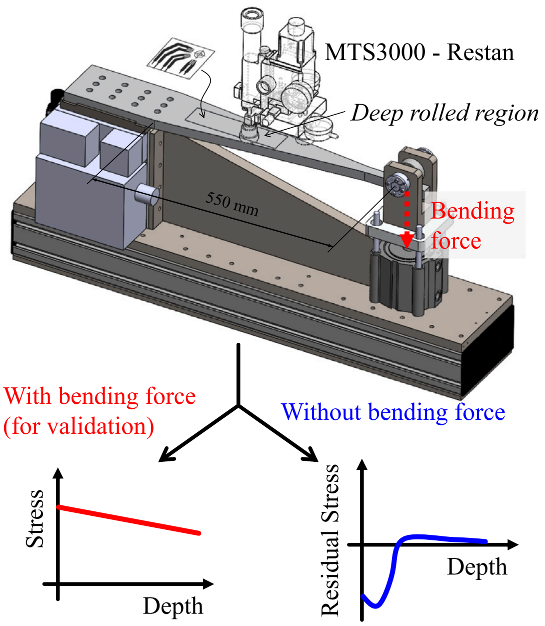

**Fig. 4.** Test bench used for *validated* residual stress identification via the application of a known bending stress distribution.

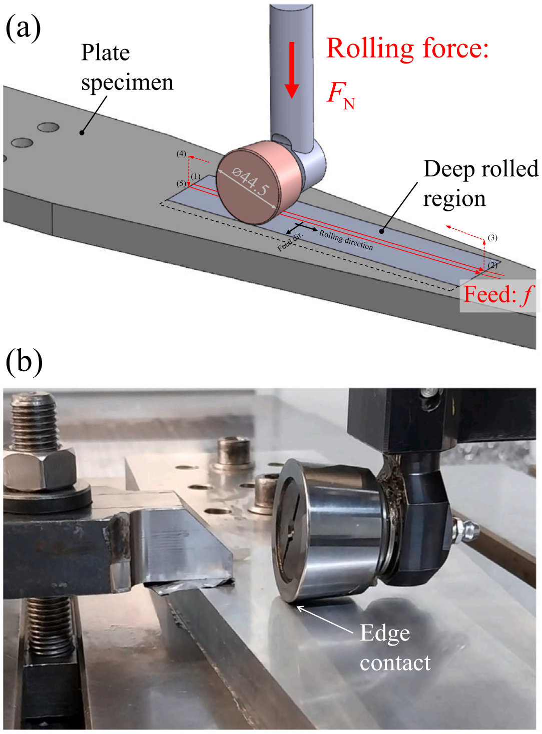

**Fig. 5.** (a) Nomenclature used in the deep rolling process; (b) Photo of the tool in action on the aluminum specimen.

force indicator. The desired force was achieved by controlling the tool-holder displacement and using disk springs to introduce compliance, thereby ensuring consistent normal force $F_N$.

The indenter makes edge contact with the surface – rather than line contact – encouraging localized plasticity while requiring lower force, which is advantageous for machining centers. Each roller path was linear; after each pass, the tool was lifted and repositioned with an offset, known as the feed length $f$. Thus, the two parameters defining treatment intensity are the normal force $F_N$ and the feed $f$. Consistently with previous works [52,53], the parameters were set to $F_N = 150\,\mathrm{N}$ and $f = 0.1\,\mathrm{mm}$, resulting in a typical deep rolling residual stress distribution, similar to that of large-shot peening [54,55]. Deep rolling also produces slightly deeper affected layers and superior surface finish. Notably, the resulting stress state is non-equibiaxial: the compressive stresses along the feed direction exceed those along the rolling direction—an advantage for the evaluation of residual stress identification methods.

### 3.2. Traditional strain gauge measurements

To compare HDM-DIC measurements with established methods, residual stress evaluation was performed using a strain gauge rosette on the deep-rolled specimen mounted in the test bench. The test bench features a pneumatic actuator capable of applying and removing a known bending load without disassembling any components. Bending stress identification was based on two sets of measurements—taken in loaded and unloaded conditions. Hole-drilling was carried out in both states, and relaxed strain data were recorded for each step.

Assuming linear elasticity, the difference between the loaded and unloaded measurements isolates the applied bending stress, while the unloaded-state data correspond to the residual stresses in the specimen. Thus, the residual stresses are obtained directly from the unloaded configuration, and the bending-induced stress distribution is inferred from the differences.

This method enables *simultaneous measurement* of both residual and bending-induced relaxed strains using the same experimental setup. Shared error sources – such as hole eccentricity, surface irregularities, incorrect zero-depth identification, or inaccurate gauge factors – affect both measurements equally. If systematic errors are absent and random errors are controlled, the identified bending stress distribution should reliably represent the applied load within a reasonable confidence interval.

An HBM RY61K strain rosette was used. The hole was drilled with a $1.8\,\mathrm{mm}$ inverted cone bit using a SINT Technology Restan system powered by an air turbine at over $300{,}000\,\mathrm{rpm}$. Drilling reached a maximum depth of $1.3\,\mathrm{mm}$ in 130 increments of $0.01\,\mathrm{mm}$. This highly refined drilling scheme was deliberately chosen to maximize the measurement quality (as described in [26,27]), at the expense of the test duration.

After drilling, hole diameter and eccentricity were measured with an optical microscope (integrated into the Restan system); a 1.96 mm hole with negligible eccentricity was detected. Stress distributions were computed using calibration coefficients from [31,32,56], with a linear splines stress basis, and with Tikhonov regularization [26] complemented by the Morozov discrepancy principle [27], in line with ASTM E837 best practices.

### 3.3. DIC setup for hole-drilling

The hole-drilling method performed with strain gauges requires a well-calibrated incremental drilling process tailored to the expected stress gradient, even when regularization is applied. Similarly, HDM-DIC requires incremental drilling, although images contain millions of sensors (pixels). Crucially, this approach demands highly accurate repositioning of both the camera and spindle after each increment.

One solution is to use dedicated experimental rigs [24,57,58]. Alternatively, as adopted here, a computerized numerical control (CNC) machine tool offers high positioning accuracy through its Cartesian motion system. A machining center is ideal: it uses only three translational axes and can drill holes and reposition the camera automatically. Positioning repeatability was estimated at a few microns—suitable for this application.

As shown in Fig. 6, both the drill bit and the camera were mounted on the CNC machine. A rigid frame was attached to the stator part of the spindle – movable along X, Y, Z, but non-rotating – on which the

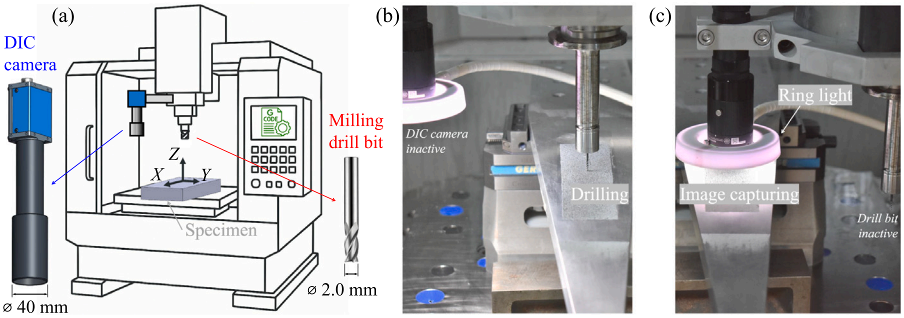

**Fig. 6.** (a) Camera and drill setup on CNC machine; (b) Drill bit aligned for a drilling step; (c) Camera aligned to capture post-drilling displacement field.

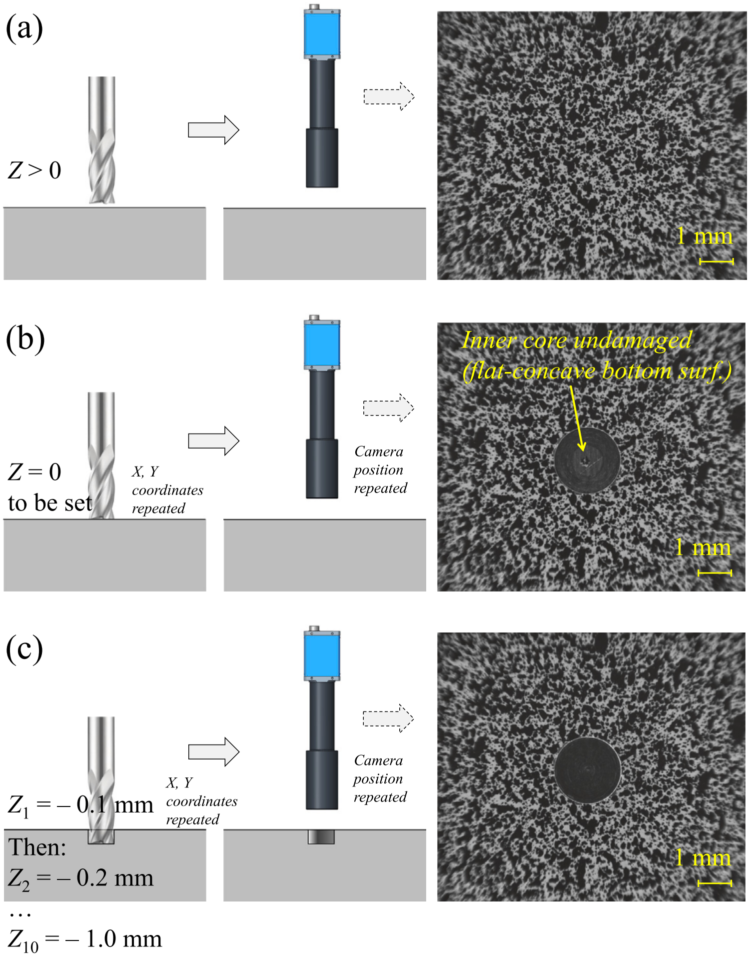

**Fig. 7.** (a) Specimen surface before drilling; (b) Surface after initial contact, showing central point of the hole; (c) Subsequent images at increasing depths.

camera was fixed. This ensured a consistent distance vector between the camera and tool tip. After each drill increment, the tool moved away and the camera returned to its exact position. The workspace offered consistent lighting conditions although it was relatively dark, so a ring light was added at the lens tip for uniform illumination.

The acquisition sequence is shown in Fig. 7. Defining the Z-axis zero position relative to the plate surface is critical [50]. A rough alignment was first made with $Z > 0$. The camera was positioned to focus on the hole area. Initially, no surface marks were visible (Fig. 7a). The bit was then rotated and lowered incrementally (in $10\,\mu\text{m}$ steps), with the camera checking for contact after each step. As the first signs of contact appeared, that depth was set as zero (Fig. 7b). The drill bit's central recess allowed us to observe an undamaged central area, confirming minimal material removal.

Once the zero was set, drilling proceeded in $0.1\,\text{mm}$ steps, with images captured at each increment (Fig. 7c), up to a nominal depth of $1.0\,\text{mm}$. Final hole depth was measured at $0.987\,\text{mm}$ using a coordinate measuring machine (Zeiss Calypso), and diameter was $2.015\,\text{mm}$, slightly larger than the nominal $2.000\,\text{mm}$. These small deviations had negligible effects, though they were accounted for in the calculations.

In the post-processing phase, we took the reference image and identify the center and radius (in pixels) of the hole using a Hough Transform, natively implemented in the `OpenCV` library [45]. Subsequently, we processed all images and selected only the pixels with

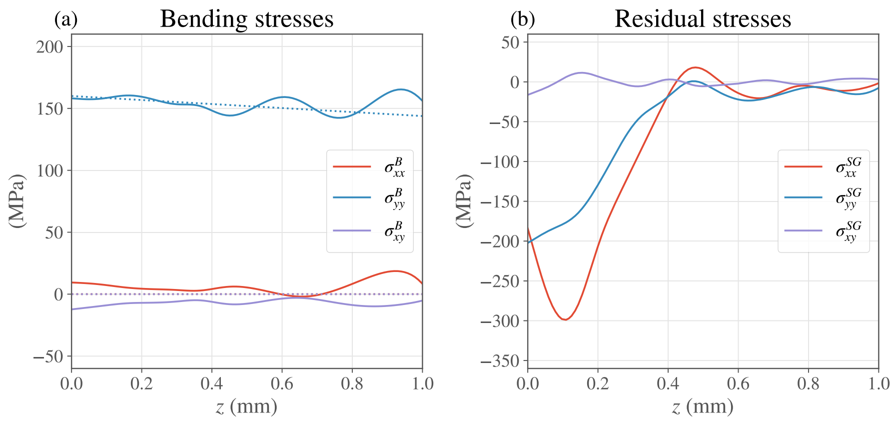

**Fig. 8.** (a) Bending stress distributions identified with the strain rosette on the test bench (solid lines) compared with the actually applied stresses (dashed lines). The identified stresses correspond very closely to the applied ones, providing evidence of a proper experimental setup. (b) Residual stress distributions identified by means of the same strain gauge rosette.

radial coordinates between 1.1 and 2.1 times the hole radius, in order to capture the largest intensity displacements caused by the introduction of the hole [59].

## 4. Results and discussion

### 4.1. Classic strain rosette measurements

The test bench was first employed to validate the residual stress measurement performed using the classical hole-drilling method formalism based on the strain gauge rosette. In Fig. 8a, the identified bending stress induced by the external actuator is shown alongside the corresponding applied values; the two are in agreement apart from the typical uncertainties of the hole-drilling method. In particular, the usual surface biases due to imperfect identification of the zero-depth reference point [50] are absent, and the trends are captured with very high accuracy.

Using the data obtained from the same physical hole – but corresponding to the absence of the externally applied load – we obtain the distribution of residual stresses actually present on the specimen surface. The results are shown in Fig. 8b. Some characteristic features of the residual stresses induced by deep rolling treatments can be observed [52], namely, that they are compressive but with a greater magnitude in the feed direction of the tool and a smaller magnitude in the rolling direction. The residual stresses are confined in depth and decay almost completely at approximately 0.4 mm below the specimen surface, beyond which they are essentially negligible.

### 4.2. DIC measurements

Using the setup on the CNC machine described in Section 3, the identification of the residual stresses was repeated with the proposed DIC algorithm based on the images acquired before and after each drilling step. In an initial solution of the problem without introducing Tikhonov regularization, it becomes evident that direct inversion leads to highly noisy results (see, for example, the lower levels of regularization in Fig. 10).

The L-curve method is therefore employed to select an appropriate level of regularization; indeed, Fig. 9b shows the L-curve obtained for the problem under analysis. It is particularly informative to conduct a visual comparison among several solutions sampled around the corner of the L-curve, which is used as the criterion for selecting a regularization level deemed optimal. Also in Fig. 9b, the points of the L-curve corresponding to a logarithmic range of $\alpha$ values between 0.001 and 100 are reported. In Fig. 10, the corresponding solutions are presented and compared with the measurement obtained from the strain gauges.

There exists a range of $\alpha$ values, approximately between 0.1 and 1, for which the solutions obtained with the strain gauge rosette and with DIC are particularly comparable. This observation is quantitatively verified in Fig. 9a, where the root mean square (RMS) difference between the two solutions at the DIC calculation points, i.e., $\sqrt{\frac{1}{n}\sum_{i=1}^{n}\left(\sigma^{DIC}(z_i)-\sigma^{SG}(z_i)\right)^2}$, is plotted as a function of $\alpha$. While the L-curve corner criterion yields an optimal $\alpha_{\mathrm{L}}$ of 0.24, the $\alpha_{\mathrm{opt}}$ that actually minimizes this difference is equal to 0.33. The rather limited discrepancies between the two corresponding solutions are shown in Fig. 11, demonstrating a region of relative numerical stability where the solution is not highly sensitive to the specific value of $\alpha$.

To demonstrate the generality of the proposed approach, which is agnostic with respect to the chosen stress basis, we repeat the residual stress calculation from scratch using DIC with different stress bases. In Fig. 12a, the residual stresses identified using a piece-wise constant function basis (i.e., that of the integral method) are presented, while Fig. 12b shows the corresponding solution obtained with a basis composed of fourth-order polynomials, a method known as the Power series method.

### 4.3. On the Morozov discrepancy principle

The behavior of the residuals as a function of $\alpha$, as observed in Fig. 9b, allows us to further elaborate on why the Morozov discrepancy principle cannot be successfully applied in this case to determine an appropriate level of regularization, as is commonly done with strain gauges and as prescribed in ASTM E837. The Morozov discrepancy principle requires, as input, an estimate of the measurement error associated with the data used to infer the residual stresses. In fact, within the tested range of $\alpha$ values – which spans from an under-regularized solution to one that is clearly over-regularized (see Fig. 10) – the value of the residuals changes by an amount negligible compared to the precision with which this error could be experimentally estimated a priori.

The reason for this lies in the physical nature of what actually generates the observed residual values, which are, in effect, the remaining misfit between the deformed images reconstructed from the reference image – using the identified displacement fields – and the deformed images captured experimentally. For example, see Fig. 13 for the displacement fields identified in this experimental validation (with rigid-body motion artifacts removed), and Fig. 14 for the pixel-wise residuals computed over all pixels where the correlation was performed.

It can be observed that the residuals are concentrated in a small fraction of pixels where the intensity differences are particularly high (the pixel intensity is expressed in 8-bit unsigned integers, i.e., ranging

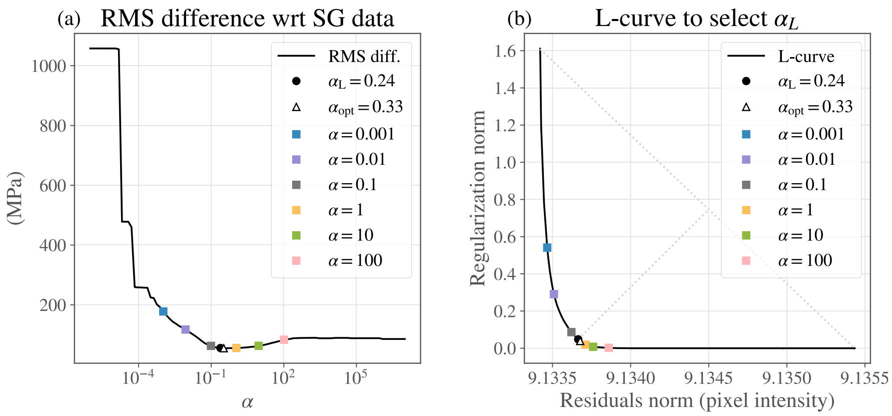

**Fig. 9.** (a) RMS difference between the solution obtained with the strain gauge and the DIC solution as a function of the regularization parameter $\alpha$; the L-curve criterion selects a value of $\alpha$ very close to the minimum of this difference. This is interpreted positively, under the assumption that the measurement performed with the strain gauges represents a state-of-the-art reference. (b) Plot of the L-curve for the experimental case under examination. Several values of $\alpha$ and their corresponding points on the L-curve are reported. Additionally, the point $\alpha_L = 0.24$ (which corresponds to the maximum distance from the line connecting the endpoints of the L-curve) and the theoretically optimal $\alpha_{opt} = 0.33$ are indicated.

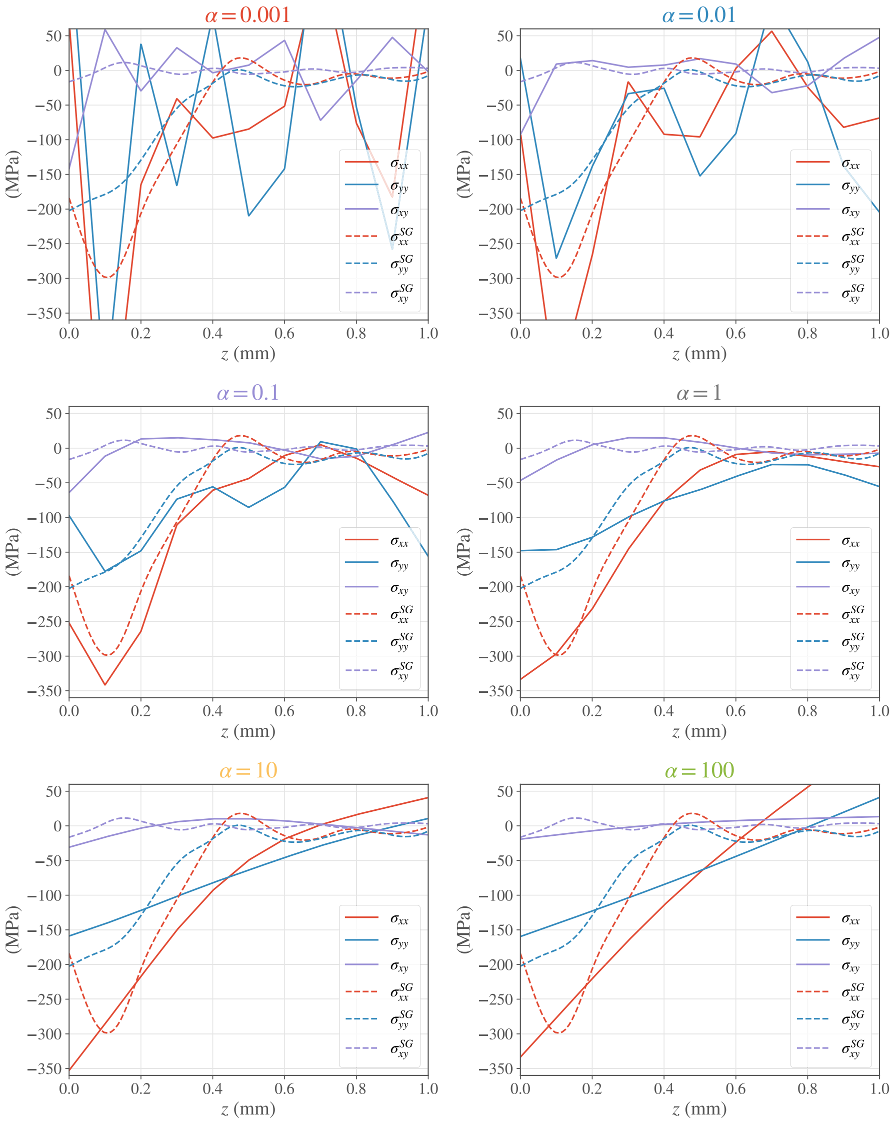

**Fig. 10.** Solutions of the inverse problem corresponding to increasing values of the regularization parameter $\alpha$. The titles of the subplots are color-coded according to the corresponding points in Fig. 9.

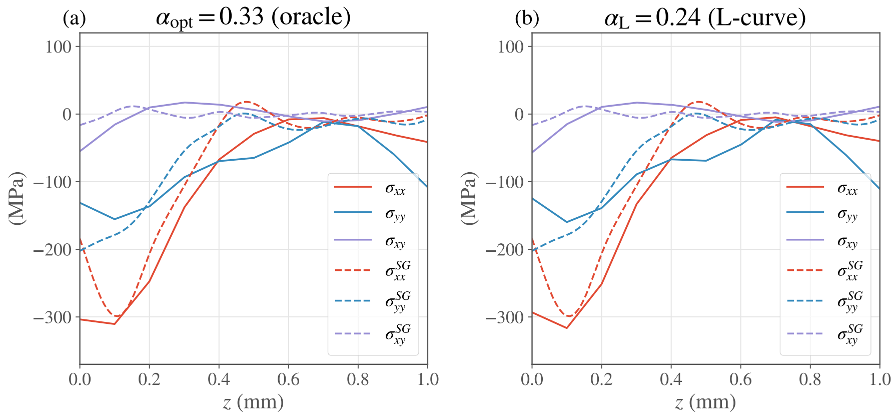

**Fig. 11.** (a) Residual stresses identified using DIC (solid lines) and subsequently regularized so as to minimize the mean squared deviation from the results obtained with strain gauge rosettes (dashed lines). In a practical context (without validation by strain gauges), this level of regularization would be unknown and is therefore referred to as “oracle” regularization. (b) Residual stresses identified using DIC and regularized according to the L-curve criterion (solid lines), compared with the results obtained from strain gauge rosettes (dashed lines).

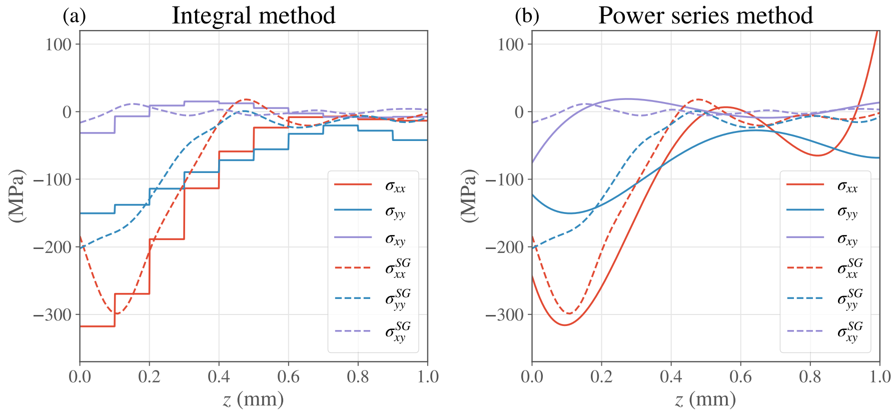

**Fig. 12.** Application of the proposed algorithm to other stress bases: (a) integral method, (b) power series method employing fourth-order polynomials.

from 0 to 255). These pixels are distributed in an apparently random manner and over a spatial scale much smaller than that on which the identified displacement fields vary, which exhibit a high degree of smoothness, in according with Saint Venant’s principle [60]. They primarily arise from machining debris – despite the area being blown with compressed air after each drilling step – and from local damage to small regions of the paint layer.

This means that an RMS residual of 9 in pixel intensity, as observed in the L-curve of Fig. 9, actually originates from a relatively small fraction of pixels where the residual is an order of magnitude higher. For these pixels, the overall residual is relatively independent of the identified displacement fields. In contrast, the displacement fields primarily govern the much lower residuals in the majority of the other pixels; however, since these are combined quadratically with the high-residual pixels, their influence on the total RMS residual is rather limited.

Recall that the rationale behind the Morozov discrepancy principle [26,27] is to acknowledge that, if the measurements are affected by a known error, it is counterproductive to seek a perfect fit between experimental and simulated data, as this will almost certainly result in overfitting. Instead, the principle suggests increasing the regularization parameter until the RMS residual matches the expected RMS measurement error.

In measurements performed with strain rosettes, this approach is particularly effective: the random error on each gauge is readily modeled as a distribution of independent and identically distributed random variables whose characteristics can be estimated from the data, as specified in ASTM E837, or even known a priori for a given measurement setup—the random error on a strain gauge measurement is typically on the order of 1 $\mu\varepsilon$. For $\alpha = 0$, it is possible to obtain a perfect fit of the strain measurements with zero residual (at least in the “square” implementation of the integral method); $\alpha$ can be increased until the residual reaches its expected value; in this context, everything functions as intended.

By contrast, in DIC measurements, even in the absence of any regularization, the RMS residual is already larger than the uncertainty on a single pixel due to the camera sensor’s measurement noise. The latter can be estimated by repeatedly capturing the same image and analyzing the pixel-wise variation; with our setup, we obtained an uncertainty of approximately 4 intensity levels, which is significantly smaller than the observed residual of 9.

At this point, it is intuitive to consider excluding such outlier pixels from the computation of the residuals; however, this would not result in a straightforward application of Morozov’s discrepancy principle. In fact, the number of degrees of freedom in the problem (i.e., the dimensionality of $\mathbf{s}$) is orders of magnitude smaller than the total number of pixels (on the order of $10^6$ per image). Consequently, even with $\alpha = 0$, the residual would essentially coincide with the contribution from measurement error alone; this does not correspond to a physically plausible solution (see Fig. 10).

Given the uncertainties introduced by removing outlier pixels, by estimating the random measurement error, and considering how sensitive the Morozov discrepancy principle is to the assumed error level [27],

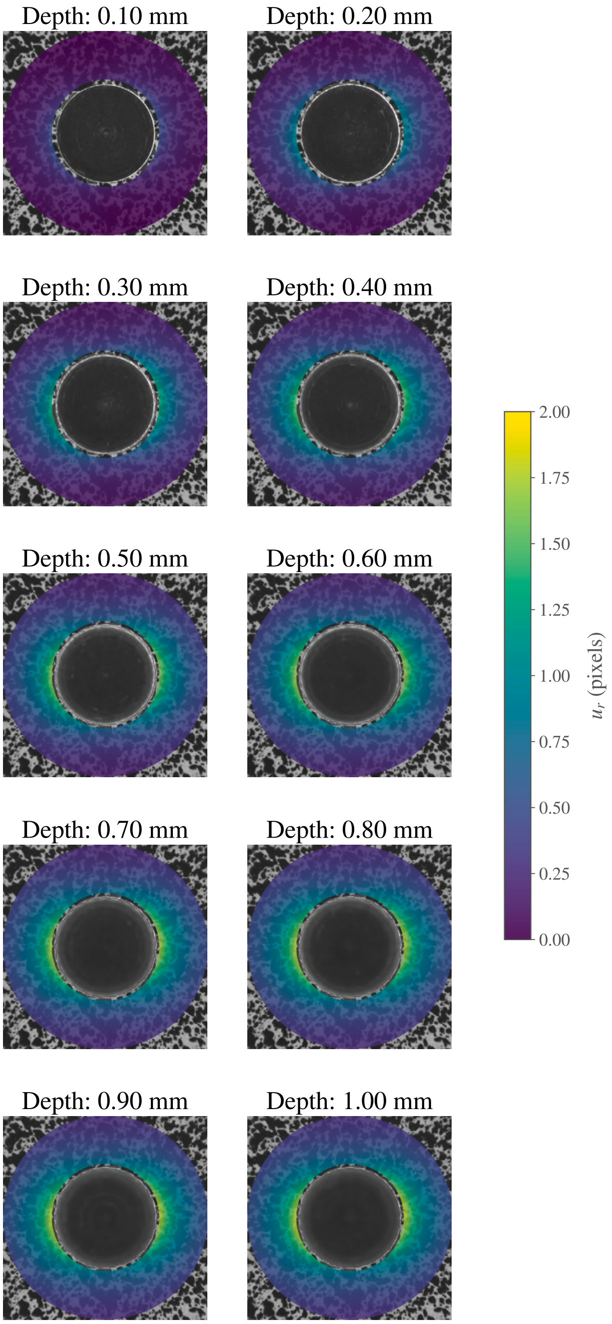

**Fig. 13.** Sequence of deformed images provided as input to the DIC technique, with superimposed radial displacement fields $u_r$ (expressed in pixels) identified through the inverse problem, excluding rigid-body motion artifacts. Although imperceptible to the naked eye, a progressive relaxation of the material around the hole becomes evident as its depth increases.

we do not believe it is possible to obtain robust results with this approach. Instead, we recommend the use of alternative heuristics for determining $\alpha$, such as the proposed L-curve, even just to obtain an initial estimate of $\alpha$, which can then be manually adjusted according to the experience of the residual stress analyst.

### 4.4. Super-resolution along depth

As anticipated in Section 2.5, we test the possibility of overcoming a classical limitation of the hole-drilling method. We repeat the identification of the residual stresses on the deep-rolled specimen, maintaining the same stress resolution in depth (i.e., 0.1 mm) but using only a subset of the acquired images, thus simulating a scenario in which fewer drilling steps were performed than the desired resolution. We investigate two super-resolution ratios: 1:2 (one image every 0.2 mm) and 1:5 (one image every 0.5 mm). The results are presented, respectively, in Fig. 15a and Fig. 15b.

It is interesting to note that the 1:2 ratio – which effectively halves the test duration – results in a virtually negligible deterioration in the quality of the solution, indicating that this level of super-resolution is

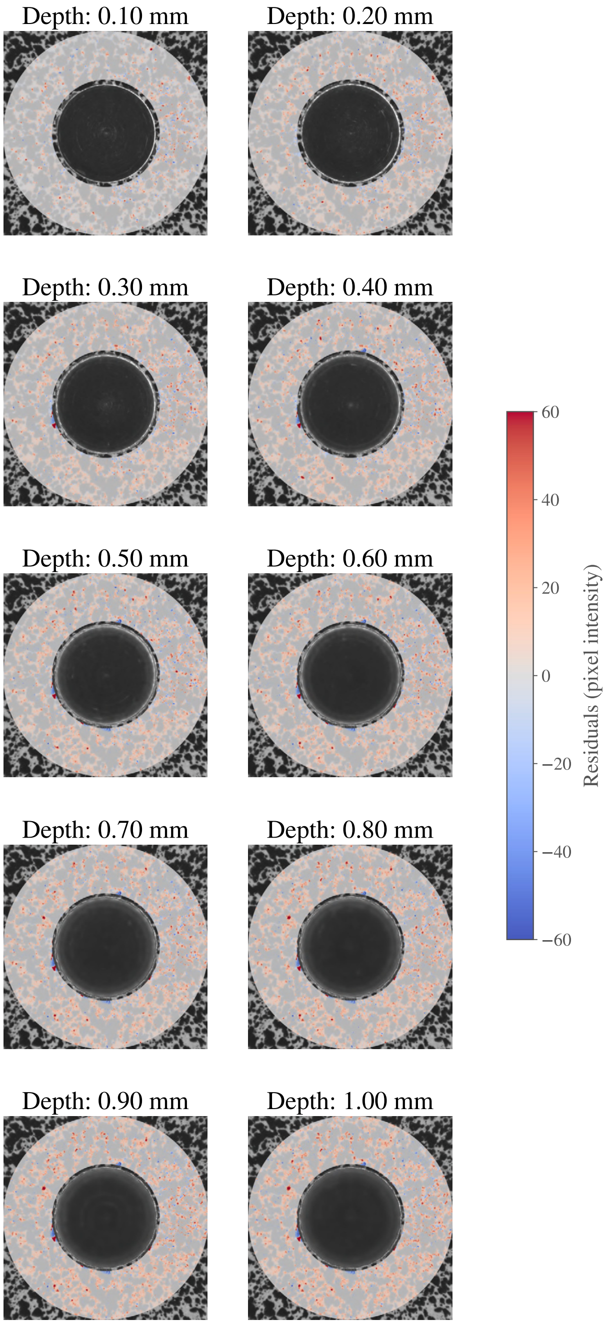

**Fig. 14.** Pixel-wise residuals between the experimental deformed images and those reconstructed by applying the identified displacement fields to the reference image, expressed as the difference in pixel intensities (0–255). It is evident that these differences are concentrated on spatial scales much smaller than those over which the displacement fields induced by the introduction of the hole vary; in fact, they arise primarily from machining debris and local damage to the paint layer.

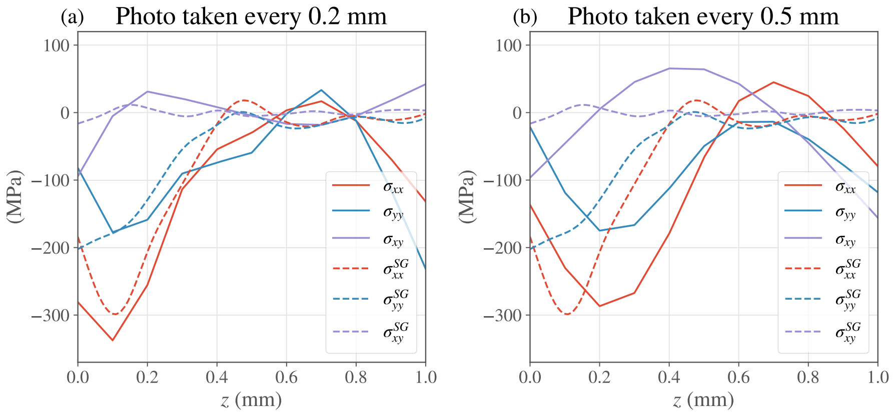

**Fig. 15.** Inverse problem solution obtained using the same number of stress points but assuming a smaller number of images than stress values. (a) Solution obtained with 5 deformed images, acquired every 0.2 mm. (b) Solution obtained with 2 deformed images, acquired every 0.5 mm. The degradation of the solution is indeed very limited in case (a), indicating that a super-resolution factor of 2 with respect to the number of images is technologically feasible. The case (b) involving only two images is also of interest for rapid stress evaluations, although the quality of the solution is clearly lower.

technologically achievable with the proposed setup. Equally noteworthy is that the more extreme 1:5 ratio, implemented *using only three images in total* (a reference image, one at 0.5 mm depth, and one at 1 mm), is still able to capture the general trend of the solution, albeit with an expected loss of spatial resolution. In particular, it can be observed that the method no longer discriminates accurately the precise depth at which the stresses decay to zero.

It is also rather remarkable that, even without any intermediate images between 0 and 0.5 mm, the method can still recover the typical stress profile in the feed direction, showing a slightly lower stress at the surface that reaches a sub-surface peak before decaying towards zero. Although it is clear that acquiring more images improves the solution quality, industrial constraints often require a trade-off between accuracy and test duration—just as is already the case in hole-drilling evaluations with strain rosettes, where not every user can afford to perform measurements with drilling steps as small as 0.01 mm, as would prove beneficial to the solution quality [26,27].

In this regard, the capability of full-field methods to extract meaningful results even from sparse data opens particularly promising perspectives. Rather than a fixed objective, we propose this as a challenge to the residual stress community: to retrieve a residual stress profile with significant depth-dependent variation using only two images—one reference image and one acquired after the drilling operation.

## 5. Conclusion

In the present work, we propose a global Eulerian DIC algorithm for the identification of residual stresses based on images acquired at increasing hole depths, complemented by a criterion for selecting the regularization parameter related to Tikhonov regularization. We summarize the main findings of this work:

- The current state of technology enables the DIC technique to achieve residual stress identifications comparable to those obtained with strain rosettes, thanks in part to the implementation of practically proven tools such as Tikhonov regularization.
- In order to ensure accurate repositioning of the milling tool and the camera – necessary for capturing a series of images at incremental depths – we designed an integrated system within a CNC machine that enables the entire test to be carried out with automated procedures.
- While the Morozov discrepancy principle is particularly effective for strain rosette measurements, its application to DIC data is both unclear and challenging. As an alternative, we propose using the L-curve tool as a heuristic method for selecting the optimal value of the regularization parameter $\alpha$.
- To the authors' best knowledge, we demonstrate for the first time that super-resolution in depth is practically achievable, reaching a 1:2 ratio without a noticeable decrease in solution quality, thereby benefiting the test duration. Instead, we observe a more pronounced error as the super-resolution ratio increases.

## CRediT authorship contribution statement

**Tommaso Grossi:** Writing – review & editing, Writing – original draft, Validation, Methodology, Investigation, Data curation, Conceptualization. **Paolo Neri:** Writing – review & editing, Writing – original draft, Validation, Methodology, Investigation, Data curation, Conceptualization. **Ciro Santus:** Writing – review & editing, Writing – original draft, Validation, Methodology, Investigation, Data curation, Conceptualization.

## Funding

This work was partially supported by Università di Pisa with Grant PRA_2022_65.

## Declaration of competing interest

The authors declare that they have no known competing financial interests or personal relationships that could have appeared to influence the work reported in this paper.

## Appendix. Scale-invariance of the identification of the L-curve corner

Let $(x(\alpha), y(\alpha))$ be a parametric expression of the L-curve, obtained as a function of the regularization parameter $\alpha$. We deliberately do not specify a fixed expression for $x$ and $y$, to allow for arbitrary scalings.

Define $\left(a_0, b_0\right) \triangleq (x(0), y(0))$ and $\left(a_\infty, b_\infty\right) \triangleq (x(\infty), y(\infty))$ as the first and last points of the L-curve; in practice, the last point is obtained with a high-enough value of $\alpha$, such that the residual stress solution is essentially linear.

The line going from $\left(a_0, b_0\right)$ to $\left(a_\infty, b_\infty\right)$ follows the Cartesian equation:

$$(b_\infty - b_0)(x - a_0) - (a_\infty - a_0)(y - b_0) = 0 \tag{A.1}$$

The proposed criterion seeks the point of the L-curve that maximizes the distance with respect to that line, which can be expressed as:

$$d\left(x(\alpha), y(\alpha)\right) = \frac{\left|(b_\infty - b_0)(x(\alpha) - a_0) - (a_\infty - a_0)(y(\alpha) - b_0)\right|}{(b_\infty - b_0)^2 + (a_\infty - a_0)^2} \tag{A.2}$$

Since $(x(\alpha), y(\alpha))$ belongs to the half-plane "under" the line defined by Eq. (A.1), we know in advance that $(b_\infty - b_0)(x(\alpha) - a_0) - (a_\infty - a_0)(y(\alpha) - b_0) > 0$, so we can conveniently remove the absolute value in Eq. (A.2), obtaining:

$$d\left(x(\alpha), y(\alpha)\right) = \frac{(b_\infty - b_0)(x(\alpha) - a_0) - (a_\infty - a_0)(y(\alpha) - b_0)}{(b_\infty - b_0)^2 + (a_\infty - a_0)^2} \tag{A.3}$$

Since the denominator in Eq. (A.3) does not depend on $\alpha$, the maximizer of Eq. (A.3) equals that of the numerator:

$$\arg\max_{\alpha} d\left(x(\alpha), y(\alpha)\right) = \arg\max_{\alpha} \left[(b_\infty - b_0)(x(\alpha) - a_0) - (a_\infty - a_0)(y(\alpha) - b_0)\right] \tag{A.4}$$

which can be easily found among the points that satisfy the first-order condition:

$$(b_\infty - b_0)\frac{d\,x(\alpha)}{d\alpha} - (a_\infty - a_0)\frac{d\,y(\alpha)}{d\alpha} = 0 \tag{A.5}$$

that, in turn, is equivalent to:

$$\frac{d\,y(\alpha)}{d\,x(\alpha)} = \frac{b_\infty - b_0}{a_\infty - a_0} \tag{A.6}$$

Eq. (A.6) has an intuitive geometrical meaning: the stationary points of the distance with respect to the line connecting the first and last points of the L-curve are those where the local tangent vector has the same direction as the line itself. Since the L-curve is inherently built as a twice-differentiable parametric function – we interpolate it along a finite set of data points – and the distance is bounded, an optimal value $\alpha = \alpha_{\mathrm{L}}$ always exists. Knowing that the L-curve can be seen as a convex function in the $xy$ plane [42], the optimal value $\alpha_{\mathrm{L}}$ is also unique.

Now, define $x'(\alpha) \triangleq \lambda_x x(\alpha) + c_x$ and $y'(\alpha) \triangleq \lambda_y y(\alpha) + c_y$, for real positive scaling factors $\lambda_x$ and $\lambda_y$, and real shifts $c_x$ and $c_y$. Accordingly, the first and last points will be $\left(a'_0, b'_0\right) = \left(\lambda_x a_0 + c_x, \lambda_y b_0 + c_y\right)$ and $\left(a'_\infty, b'_\infty\right) = \left(\lambda_x a_\infty + c_x, \lambda_y b_\infty + c_y\right)$.

Assume that $\alpha = \alpha_{\mathrm{L}}$ is an optimal point in the scaled coordinates:

$$\alpha_{\mathrm{L}} = \arg\max_{\alpha} \left[(b'_\infty - b'_0)(x'(\alpha) - a'_0) - (a'_\infty - a'_0)(y'(\alpha) - b'_0)\right] \tag{A.7}$$

We also have:

$$\begin{aligned}
&(b'_\infty - b'_0)(x'(\alpha) - a'_0) - (a'_\infty - a'_0)(y'(\alpha) - b'_0) = \\
&\quad = \lambda_x \lambda_y (b_\infty - b_0)(x(\alpha) - a_0) - \lambda_x \lambda_y (a_\infty - a_0)(y(\alpha) - b_0) \\
&\quad = \lambda_x \lambda_y \left[(b_\infty - b_0)(x(\alpha) - a_0) - (a_\infty - a_0)(y(\alpha) - b_0)\right]
\end{aligned} \tag{A.8}$$

where all shifts $c_x$ and $c_y$ get canceled out. Eq. (A.8) shows that, as $\alpha$ varies, the distance to be maximized in one coordinate system is simply a multiple of the distance to be maximized in another (scaled) coordinate system. Therefore, if $\alpha_{\mathrm{L}}$ maximizes the target distance in the transformed coordinates, it also maximizes the target distance in the original coordinates, and vice-versa.

## Data availability

Data will be made available on request.

## References

[1] J. Mathar, Determination of initial stresses by measuring the deformations around drilled holes, Trans. Am. Soc. Mech. Eng. 56 (3) (1934) 249–254, ISBN: 0097-6822 Publisher: American Society of Mechanical Engineers.

[2] American Society for Testing and Materials, Test method for determining residual stresses by the hole-drilling strain-gage method, West Conshohocken, PA (2020) http://dx.doi.org/10.1520/E0837-20.

[3] G.S. Schajer, Application of finite element calculations to residual stress measurements, J. Eng. Mater. Technol. 103 (2) (1981) 157–163, http://dx.doi.org/10.1115/1.3224988.

[4] G.S. Schajer, Measurement of non-uniform residual stresses using the hole-drilling method. part I stress calculation procedures, J. Eng. Mater. Technol. 110 (4) (1988) 338–343, http://dx.doi.org/10.1115/1.3226059.

[5] G.S. Schajer, Measurement of non-uniform residual stresses using the hole-drilling method. part II practical application of the integral method, J. Eng. Mater. Technol. 110 (4) (1988) 344–349, http://dx.doi.org/10.1115/1.3226060.

[6] G.S. Schajer, Practical Residual Stress Measurement Methods, John Wiley & Sons, 2013.

[7] N.J. Rendler, I. Vigness, Hole-drilling strain-gage method of measuring residual stresses: Authors indicate that this method permits the magnitudes and principal directions of residual stresses at the hole location to be determined, Exp. Mech. 6 (12) (1966) 577–586, http://dx.doi.org/10.1007/BF02326825.

[8] M. Steinzig, E. Ponslet, Residual stress measurement using the hole drilling method and laser speckle interferometry: Part 1, Exp. Tech. 27 (3) (2003) 43–46, http://dx.doi.org/10.1111/j.1747-1567.2003.tb00114.x.

[9] G.S. Schajer, M. Steinzig, Full-field calculation of hole drilling residual stresses from electronic speckle pattern interferometry data, Exp. Mech. 45 (6) (2005) 526–532, http://dx.doi.org/10.1007/BF02427906.

[10] G.S. Schajer, M. Steinzig, Dual-axis hole-drilling ESPI residual stress measurements, J. Eng. Mater. Technol. 132 (1) (2010) 011007, http://dx.doi.org/10.1115/1.3184035.

[11] A. Baldi, F. Bertolino, Sensitivity analysis of full field methods for residual stress measurement, Opt. Lasers Eng. 45 (5) (2007) 651–660, http://dx.doi.org/10.1016/j.optlaseng.2006.08.010.

[12] A. Baldi, Residual stress measurement using hole drilling and integrated digital image correlation techniques, Exp. Mech. 54 (3) (2014) 379–391, http://dx.doi.org/10.1007/s11340-013-9814-6.

[13] J.S. Harrington, G.S. Schajer, Measurement of structural stresses by hole-drilling and DIC, Exp. Mech. 57 (4) (2017) 559–567, http://dx.doi.org/10.1007/s11340-016-0247-x.

[14] A. Baldi, On the implementation of the integral method for residual stress measurement by integrated digital image correlation, Exp. Mech. 59 (7) (2019) 1007–1020, http://dx.doi.org/10.1007/s11340-019-00503-5.

[15] Y. Peng, J. Zhao, L.-s. Chen, J. Dong, Residual stress measurement combining blind-hole drilling and digital image correlation approach, J. Constr. Steel Res. 176 (2021) 106346, http://dx.doi.org/10.1016/j.jcsr.2020.106346.

[16] D.V. Nelson, A. Makino, T. Schmidt, Residual stress determination using hole drilling and 3D image correlation, Exp. Mech. 46 (1) (2006) 31–38, http://dx.doi.org/10.1007/s11340-006-5859-0.

[17] W.L. Gubbels, G.S. Schajer, Development of 3-D digital image correlation using a single color-camera and diffractive speckle projection, Exp. Mech. 56 (8) (2016) 1327–1337, http://dx.doi.org/10.1007/s11340-016-0173-y.

[18] M. Hagara, F. Trebuňa, M. Pástor, R. Huňady, P. Lengvarský, Analysis of the aspects of residual stresses quantification performed by 3D DIC combined with standardized hole-drilling method, Measurement 137 (2019) 238–256, http://dx.doi.org/10.1016/j.measurement.2019.01.028.

[19] H. Schreier, J.-J. Orteu, M.A. Sutton, Image correlation for shape, motion and deformation measurements: Basic concepts,theory and applications, Springer US, Boston, MA, 2009, http://dx.doi.org/10.1007/978-0-387-78747-3.

[20] J.D. Lord, D. Penn, P. Whitehead, The application of digital image correlation for measuring residual stress by incremental hole drilling, Appl. Mech. Mater. 13–14 (2008) 65–73, http://dx.doi.org/10.4028/www.scientific.net/AMM.13-14.65.

[21] G.S. Schajer, Optical hole-drilling residual stress calculations using strain gauge formalism, Exp. Mech. 61 (9) (2021) 1369–1380, http://dx.doi.org/10.1007/s11340-021-00740-7.

[22] G.S. Schajer, Compact calibration data for hole-drilling residual stress measurements in finite-thickness specimens, Exp. Mech. 60 (5) (2020) 665–678, http://dx.doi.org/10.1007/s11340-020-00587-4.

[23] G.S. Schajer, Hole-drilling residual stress profiling with automated smoothing, J. Eng. Mater. Technol. 129 (3) (2007) 440–445, http://dx.doi.org/10.1115/1.2744416.

[24] E. Arabul, A.J.G. Lunt, A novel low-cost DIC-based residual stress measurement device, Appl. Sci. 12 (14) (2022) 7233, http://dx.doi.org/10.3390/app12147233.

[25] G.S. Schajer, B. Winiarski, P.J. Withers, Hole-drilling residual stress measurement with artifact correction using full-field DIC, Exp. Mech. 53 (2) (2013) 255–265, http://dx.doi.org/10.1007/s11340-012-9626-0.

[26] M. Beghini, T. Grossi, M. Prime, C. Santus, Ill-posedness and the bias-variance tradeoff in residual stress measurement inverse solutions, Exp. Mech. 63 (3) (2023) 495–516, http://dx.doi.org/10.1007/s11340-022-00928-5.

[27] M. Beghini, T. Grossi, Towards a reliable uncertainty quantification in residual stress measurements with relaxation methods: Finding average residual stresses is a well-posed problem, Exp. Mech. (2024) http://dx.doi.org/10.1007/s11340-024-01066-w.

[28] V.A. Morozov, Methods for Solving Incorrectly Posed Problems, Springer New York, New York, NY, 1984, http://dx.doi.org/10.1007/978-1-4612-5280-1.

[29] P.C. Hansen, The L-curve and its use in the numerical treatment of inverse problems, 1999.

[30] H.F. Bueckner, Novel principle for the computation of stress intensity factors, Z. Fuer Angew. Math. Mech. 50 (9) (1970).

[31] M. Beghini, L. Bertini, L.F. Mori, Evaluating non-uniform residual stress by the hole-drilling method with concentric and eccentric holes. part II: Application of the influence functions to the inverse problem: Eccentric influence functions - part II, Strain 46 (4) (2010) 337–346, http://dx.doi.org/10.1111/j.1475-1305.2009.00684.x.

[32] M. Beghini, L. Bertini, L.F. Mori, Evaluating non-uniform residual stress by the hole-drilling method with concentric and eccentric holes. part I. definition and validation of the influence functions: Eccentric influence functions - part I, Strain 46 (4) (2010) 324–336, http://dx.doi.org/10.1111/j.1475-1305.2009.00683.x.

[33] M. Barsanti, M. Beghini, L. Bertini, B.D. Monelli, C. Santus, First-order correction to counter the effect of eccentricity on the hole-drilling integral method with strain-gage rosettes, J. Strain Anal. Eng. Des. 51 (6) (2016) 431–443, http://dx.doi.org/10.1177/0309324716649529.

[34] M. Beghini, L. Bertini, M. Cococcioni, T. Grossi, C. Santus, A. Benincasa, Regularization of hole-drilling residual stress measurements with eccentric holes: An approach with influence functions, J. Mater. Eng. Perform. (2024) http://dx.doi.org/10.1007/s11665-024-09447-x.

[35] W.H. Peters, W.F. Ranson, Digital imaging techniques in experimental stress analysis, Opt. Eng., Bellingham 21 (3) (1982) 427–431, http://dx.doi.org/10.1117/12.7972925, Publisher: SPIE.

[36] M. Sutton, W. Wolters, W. Peters, W. Ranson, S. McNeill, Determination of displacements using an improved digital correlation method, Image Vis. Comput. 1 (3) (1983) 133–139, http://dx.doi.org/10.1016/0262-8856(83)90064-1.

[37] T.C. Chu, W.F. Ranson, M.A. Sutton, Applications of digital-image-correlation techniques to experimental mechanics, Exp. Mech. 25 (3) (1985) 232–244, http://dx.doi.org/10.1007/BF02325092.

[38] J.-C. Passieux, R. Bouclier, Classic and inverse compositional Gauss-Newton in global DIC, Internat. J. Numer. Methods Engrg. 119 (6) (2019) 453–468, http://dx.doi.org/10.1002/nme.6057.

[39] C.R. Vogel, Computational Methods for Inverse Problems, SIAM, 2002.

[40] C.L. Lawson, R.J. Hanson, Solving Least Squares Problems, SIAM, 1995.

[41] P.C. Hansen, Analysis of discrete ill-posed problems by means of the L-curve, SIAM Rev. 34 (4) (1992) 561–580, http://dx.doi.org/10.1137/1034115.

[42] P.C. Hansen, Discrete Inverse Problems: Insight and Algorithms, SIAM, 2010.

[43] M. Beghini, T. Grossi, Measuring residual stresses with crack compliance methods: An Ill-posed inverse problem with a closed-form Kernel, Appl. Mech. 5 (3) (2024) 475–489, http://dx.doi.org/10.3390/applmech5030027.

[44] R.O. Duda, P.E. Hart, Use of the hough transformation to detect lines and curves in pictures, Commun. ACM 15 (1) (1972) 11–15, http://dx.doi.org/10.1145/361237.361242.

[45] G. Bradski, The opencv library, Dr. Dobb's J. Softw. Tools (2000).

[46] R. Keys, Cubic convolution interpolation for digital image processing, IEEE Trans. Acoust. Speech Signal Process. 29 (6) (1981) 1153–1160, http://dx.doi.org/10.1109/TASSP.1981.1163711.

[47] M. Beghini, T. Grossi, C. Santus, E. Valentini, A calibration bench to validate systematic error compensation strategies in hole drilling measurements, in: ICRS 11–11th International Conference on Residual Stresses, 2022, http://dx.doi.org/10.36227/techrxiv.20347788.v1.

[48] M. Beghini, T. Grossi, C. Santus, A. Torboli, A. Benincasa, M. Bandini, X-ray diffraction and hole-drilling residual stress measurements of shot peening treatments validated on a calibration bench, in: ICSP 14–14th International Conference on Shot Peening, Milan, Italy, 2022, https://www.shotpeener.com/library/pdf/2022101.pdf.

[49] M. Beghini, T. Grossi, C. Santus, L. Seralessandri, S. Gulisano, Residual stress measurements on a deep rolled aluminum specimen through X-ray diffraction and hole-drilling, validated on a calibration bench, IOP Conf. Ser.: Mater. Sci. Eng. 1275 (1) (2023) 012036, http://dx.doi.org/10.1088/1757-899X/1275/1/012036.

[50] M. Beghini, T. Grossi, C. Santus, E. Valentini, Revealing systematic errors in hole drilling measurements through a calibration bench: the case of zero-depth data, J. Theor. Comput. Appl. Mech. (2023) http://dx.doi.org/10.46298/jtcam.10080.

[51] M. Beghini, T. Grossi, C. Santus, Validation of a strain gauge rosette setup on a cantilever specimen: Application to a calibration bench for residual stresses, Mater. Today: Proc. (2023) http://dx.doi.org/10.1016/j.matpr.2023.05.505, S2214785323031371.

[52] M. Beghini, L. Bertini, B. Monelli, C. Santus, M. Bandini, Experimental parameter sensitivity analysis of residual stresses induced by deep rolling on 7075-T6 aluminium alloy, Surf. Coat. Technol. 254 (2014) 175–186, http://dx.doi.org/10.1016/j.surfcoat.2014.06.008.

[53] L. Bertini, C. Santus, Fretting fatigue tests on shrink-fit specimens and investigations into the strength enhancement induced by deep rolling, Int. J. Fatigue 81 (2015) 179–190, http://dx.doi.org/10.1016/j.ijfatigue.2015.08.007.

[54] M. Benedetti, V. Fontanari, C. Santus, M. Bandini, Notch fatigue behaviour of shot peened high-strength aluminium alloys: Experiments and predictions using a critical distance method, Int. J. Fatigue 32 (10) (2010) 1600–1611, http://dx.doi.org/10.1016/j.ijfatigue.2010.02.012.

[55] M. Benedetti, M. Pedranz, V. Fontanari, C. Menapace, M. Bandini, Enhancing plain fatigue strength in aluminum alloys through shot peening: Experimental investigations and a strain energy density interpretation, Int. J. Fatigue 184 (2024) 108299, http://dx.doi.org/10.1016/j.ijfatigue.2024.108299.

[56] M. Beghini, L. Bertini, Analytical expressions of the influence functions for accuracy and versatility improvement in the hole-drilling method, J. Strain Anal. Eng. Des. 35 (2) (2000) 125–135, http://dx.doi.org/10.1243/0309324001514071.

[57] R. Blödorn, L.A. Bonomo, M.R. Viotti, R.B. Schroeter, A. Albertazzi, Calibration coefficients determination through fem simulations for the hole-drilling method considering the real hole geometry, Exp. Tech. 41 (1) (2017) 37–44, http://dx.doi.org/10.1007/s40799-016-0152-3.

[58] M. Pástor, M. Hagara, I. Virgala, A. Kal'avský, A. Sapietová, L. Hagarová, Design of a unique device for residual stresses quantification by the drilling method combining the PhotoStress and digital image correlation, Materials 14 (2) (2021) 314, http://dx.doi.org/10.3390/ma14020314.

[59] C. Santus, P. Neri, L. Romoli, M. Cococcioni, Residual stress determination with the hole-drilling method on FDM 3D-printed precurved specimen through digital image correlation, Appl. Sci. 14 (10) (2024) 3992, http://dx.doi.org/10.3390/app14103992.

[60] R. von Mises, On saint Venant's principle, Bull. Am. Math. Soc. 51 (8) (1945) 555–562, http://dx.doi.org/10.1090/S0002-9904-1945-08394-3.